IIETA International Information and Engineering Technology Association
Advancing the World of Information and Engineering

International Journal of Heat and Technology
Vol. 43, No. 2, April, 2025, pp. 703-720
Journal homepage: http://iieta.org/journals/ijht

A Numerical Study of the Solar Air Heater Performance Using Artificial Spherical Obstacles

Ghassan Abdulameer Habeeb*, Ameer Abed Jaddoa, Jafaar Mohammed Daif Alkhasraji

Electromechanical Engineering Department, University of Technology, Baghdad 0096, Iraq

Corresponding Author Email: Ghassan.ndt.1982@gmail.com

https://doi.org/10.18280/ijht.430230

Received: 29 November 2024
Revised: 24 February 2025
Accepted: 11 March 2025
Available online: 30 April 2025

Keywords:
numerical solar air collector, absorber surface, spherical obstacles, friction factor

ABSTRACT

Solar air heaters (SAH) are required to adhere to specific standards regarding thermal efficiency and minimal internal pressure loss. We addressed the issue of significant pressure loss in SAH across five cases, designated "A" to "E", by developing an innovative SAH featuring spherical baffles (SP). We utilized computational fluid dynamics (CFD) to model the solar air heater (SAH) with solar panels (SPs), concentrating on key parameters such as heat-collecting efficiency and pressure loss magnitude. In another case, Case "E" SPs demonstrated superior performance compared to the baffle regarding heat collecting efficiency and pressure loss, as indicated by the data. An SP can improve the thermal efficiency of an SAH. The simulation of wavelengths for SPs in instance "E" at 400 mm demonstrated optimal heat collection by the SAH, achieving an efficiency of 80.65%. The investigation concentrated on the wave height of the SPs to measure wavelength. The SAH exhibited a minimum pressure loss of 19.86 Pa, a maximum heat-collecting efficiency of 60.68 percent, and a wave height of 40 mm. Higher Reynolds numbers (Re) at the air inlet were associated with improved collection efficiency and reduced internal pressure loss, whereas lower outlet temperatures corresponded with lower Re values. An accuracy of 0.897 was observed in the fitting curve for pressure loss when analyzing the imported Reynolds number and pressure loss. This study not only establishes a theoretical foundation for winter air heating but also has significant practical implications.

1. INTRODUCTION

The construction of a solar air heater (SAH) utilizing readily available materials effectively reduces fabrication costs, establishing it as a financially viable solar device [1-3]. An SAH functions by absorbing solar radiation to heat the air, thereby fulfilling the objectives of indoor heating and the drying of agricultural products [4-6]. There are many utility application models to benefit from the solar heat energy, as the flat plate collector consists of an absorbent plate, a transparent glass cover, copper tubes, and an aluminum back plate [7-9]. Furthermore, individuals utilize solar energy for energy storage purposes, including the retention of solar energy to warm buildings [10-14] or the use of glycerol and paraffin in spiral tube collectors for energy storage [15, 16]. Phase change materials (PCM) are incorporated into the air collector to enhance the operational cycle and increase the efficiency of the heater [17-19]. The approach to enhancing the conventional PCM involves modifying the extended surface structure through the application of porous materials. Extensive research has been conducted by scholars on the thermal performance of SAHs, focusing on enhancements such as the incorporation of double channels [7] and spiral flow channels [20-22] to optimize heat collection efficiency. Several researchers have enhanced the heat-absorbing plate through the development of a heat sink [23-25], a parabolic surface [26-28], and a spherical heat absorb plate [29, 30]. A significant number of researchers have focused on enhancing collection efficiency through structural improvements to the air heater, thereby optimizing the design of the SAH. This encompasses the utilization of slotted perforated corrugated plates [31, 32] as well as triangular plates [33]. Several researchers have incorporated parabolic grooves [34] and louvers [35] into the heat absorb plates to enhance the heat collection efficiency of the SAH metal foam or utilized advanced thermal materials [36]. Various researchers have advanced the concept of SAH by refining the internal structure of the conventional flat panel SAH. This includes the incorporation of circular fins [37], rough fins [38], and rectangular fins [39] into the design. The combination of these studies has the potential to enhance the heat absorption efficiency of the heat-absorbing plate, thereby improving the overall heat collection performance of the SAH. To enhance the heat collection efficiency of an SAH, researchers have incorporated various designs into the heat absorb plate, including closed-loop pulsating heat pipes, C-shaped fins, spiral fins, V-shaped fins, and porous media fins. Furthermore, certain researchers have examined various baffle types in SAHs, including folded baffles, spiral baffles [22], and hollow semi-circular baffles [23]. The findings demonstrate that the internal air temperature exceeded that of a conventional flat plate heater. The efficiency of the collection process has seen significant enhancement. The analysis conducted on the number of baffles for a spiral SAH revealed that the most effective configuration is a spiral SAH featuring two longitudinal baffles. A combination of the heat absorb plate with a PCM has been explored by certain scholars. Zayed [40] analyzed the wave-shaped corrugated solar air collector integrated with a PCM and observed an approximate 20% increase in energy efficiency when the PCM was utilized. He incorporated a PCM into the interior of the flat panel solar collector, demonstrating that the temperature increase could achieve 31% in comparison to the standard SAH.

Precedent research on baffle SAHs has predominantly focused on improving collection efficiency and maximizing daily utilization rates. The use of barriers or obstacles leads to an increase in pressure drop, which means losses in performance. Precedent researchers have focused on reducing pressure drops. The decrease in air pressure inside the SAH is an important factor, and utilizing a baffle-type SAH can improve heat utilization and airflow efficiency [41]. The folded baffle SAH demonstrates significant pressure loss, whereas the semi-circular baffle SAH can alleviate this loss, though this comes with a decrease in thermal utilization rate. This research integrates SPs into two distinct configurations of baffle SAHs. The goal is to improve the thermal efficiency of the SAH while reducing internal pressure loss by examining the parameters related to SPs [42]. This study investigates how modifications to the wavelength and wave height of SPs influence outlet temperature, collection efficiency, and pressure loss. The research further determines the ideal inlet Re through an assessment of its effects on thermal performance. This study aims to examine the elements that affect the thermal efficiency and pressure drop related to SPs in SAH. The role of sinusoidal baffles in SAHs is clear, as they improve heat utilization, reduce pressure loss, and provide a theoretical basis for air heating in winter, thus helping to maintain appropriate indoor air temperatures. This study presents the integration of SPs in SAH and analyzes their impacts.

In this study, spherical artificial obstacles were used and distributed on the absorption plate to increase air turbulence. The obstacles were distributed in several cases to test which distribution had the best improvement in SAH performance.

2. GEOMETRY AND CASES DESCRIPTIONS

The structure includes a horizontal rectangular duct measuring 150 cm in length, 80 cm in width, and 30 cm in height, along with an artificial obstacle shaped like a ball with a diameter of 2.5 cm, which is distributed on the absorber plate. A cover glass is used to encase the topside of the duct, and a wooden frame is put inside with isolation fixed on the bottom side of the absorber. For forced air flow, a blower was used in the section side, which was generated by the PV panel. Temperatures were measured by thermocouples fixed inside the duct and connected to an Arduino (digital measurement) for more accuracy. Figure 1 presents the geometry, studied cases, and baffle dimensions. The findings of five distinct analyses differing based on the positioning of the balls within the apparatus are presented here:

- Scenario A: Without balls, as the reference case.
- Scenario B: Balls mounted in the 2nd half of the air gutter “Fifty percent reposition up direction”.
- Scenario C: Balls mounted in the 1st half of the air gutter “Fifty percent reposition down direction”.
- Scenario D: Balls mounted in the middle of the air gutter “Fifty percent reposition in the middle”.
- Scenario E: Balls mounted in all the air gutters “100%”.

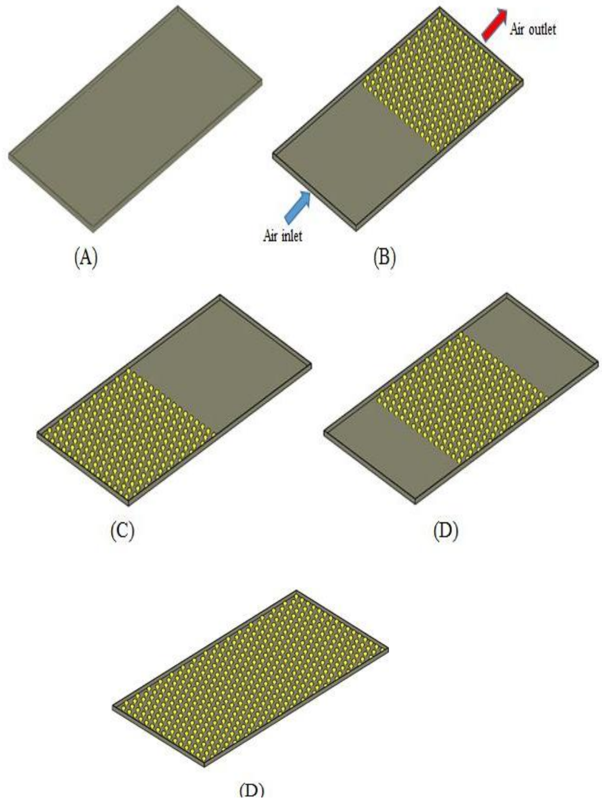

Figure 1. Investigated the dimensions of SAHs and relevant case studies: Scenario (A) Non-permeable surface; Case (B) (50% Up); Case (C) (50% Down); Case (D) (50% Middle); Case (E) (100%)

3. MESH WITH GAMBIT

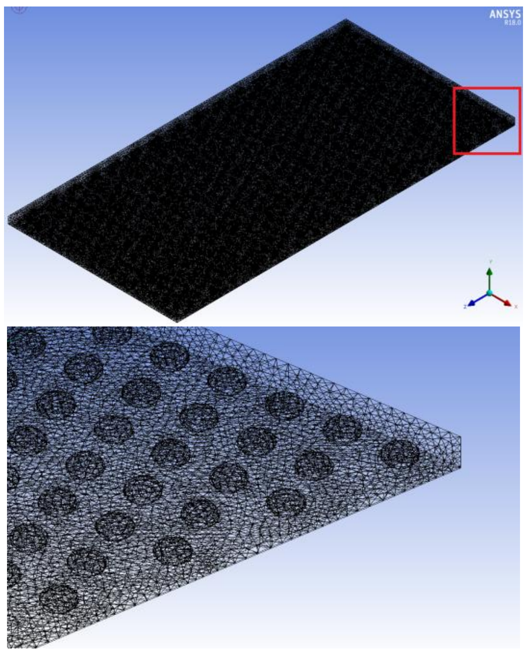

Figure 2. Grid (mesh) of the ball case

The establishment of the computational grid for the domain represents a fundamental aspect of effectively employing CFD technologies. Achieving precise and significant numerical solutions begins with the discretization of the computational domain. This step is especially critical in rapid and high-velocity flows, where pronounced gradients exist within the boundary viscous sublayer. Therefore, it is crucial to confirm that a sufficient quantity of mesh components is present within the boundary layer. The mesh for the mathematical portion of the SAH was created utilizing Ansys Fluent (version 18.0) and SolidWorks (version 16). The intricate geometry being analyzed required the implementation of a multidimensional unplanned tetrahedral mesh. Figures 2-4 present a detailed representation of the grid structure of the ball cases.

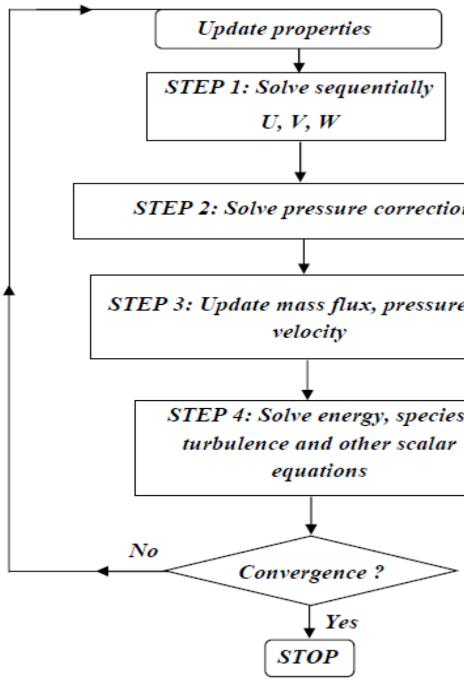

Figure 3. Steps of the segregated SIMPLE algorithm (Pressure-based solution methods)

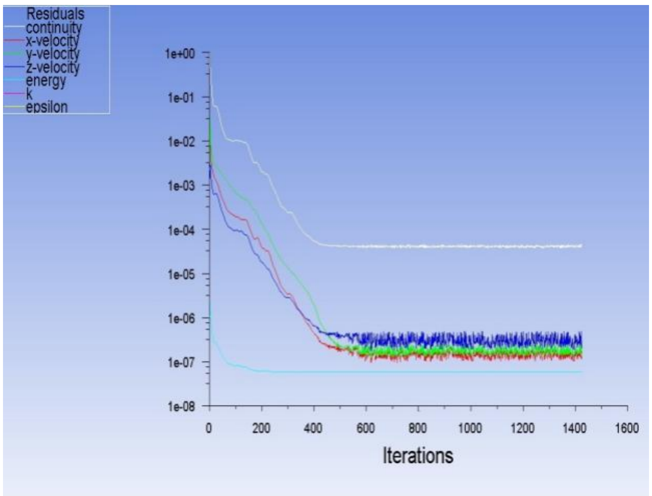

Figure 4. Curves of the convergence solution

4. BOUNDARY CONDITIONS IN GAMBIT

After defining the geometry and the mesh of the physical domain under investigation, the next step involves specifying the geometrical zones where boundary conditions will be applied. Two features of zone types (boundary conditions) are illustrated in Figure 2.

1. Types of boundaries to delineate exterior or internal limits.
2. Continuum classifications (fluid or solid) to delineate the areas of the domain.

The flow within the gutter is constrained by 2-horizontal barriers: the upper component referred to as the "cover glass" and the lower component known as the "absorber glass." The upper surface consists of translucent glass, facilitating the entry of sunlight while absorbing and reflecting a portion of it onto the lower surface. The second component is the absorber, characterized by an adiabatic wall and two adjacent side walls, which are also adiabatic. The inlet is categorized as a mass flow inlet, whereas the outflow is designated as a pressure outlet. The internal realm is characterized as being "fluid".

5. SOLVER

The examined computer model incorporates steady state, three-dimensional geometry, and Newtonian fluid dynamics. The fluid exhibits consistent characteristics, behaving precisely as a perfect gas. The characteristics are evaluated at the average temperature of the fluid within the container. In the context of forced convection, the velocities are sufficiently elevated to make gravity negligible and render all buoyancy effects inconsequential. Ansys fluent 18.0, a commercial software, is employed to solve the Navier-stokes and energy equations utilizing the finite volume process. The assumptions outlined below are utilized to produce the CFD results:

- Throughout its journey through the duct, the fluid continues to flow in a turbulent manner that is single-phase and incompressible.
- Three-dimensional dynamic fluid dynamics and thermal conduction.
- Insufficient or absent convective heat transfer (ht) resulting from radiation and natural convection among components of the computational domain.
- The thermo-physical features of the fluid (air) and the solid (aluminum) remain unchanged.

The application of the fundamental principle of thermodynamics to an incompressible Newtonian fluid result in the energy formula. The following equation represents the transport of heat within the flow field.

5.1 Continuity equation

By applying the law of mass conservation, we obtain that formula. It is expressed in vector form as follows [43]:

$$\nabla \cdot (\rho \vec{V}) = 0 \tag{1}$$

The gradient operator:

$$\nabla = \frac{\partial}{\partial x}\vec{i} + \frac{\partial}{\partial y}\vec{j} + \frac{\partial}{\partial z}\vec{k} \tag{2}$$

and the velocity vector:

$$\vec{V} = \vec{u}i + \vec{v}j + \vec{w}k \quad (3)$$

5.2 Momentum equation

The momentum equations that govern the flow of incompressible fluid take the form [44]:

$$\nabla \cdot (\rho\vec{V}\vec{V}) = -\nabla p + \nabla \cdot (\bar{\tau}) \quad (4)$$

The stress tenser $\bar{\tau}$ is given by:

$$\bar{\tau} = \mu\left[\left(\nabla\vec{V} + \nabla\vec{V}^{T}\right) - \frac{2}{3}\nabla \cdot \vec{V}I\right] \quad (5)$$

The second law of dynamics indicates that the change in momentum of a fluid particle corresponds to the sum of the external forces acting on it, and this formula is derived from that principle.

5.3 Energy equation

A Newtonian fluid, which is incompressible, is analyzed using the first law of thermodynamics to get the energy equation. Heat conduction inside the flow field is articulated by the subsequent equation:

$$\nabla \cdot (\vec{V}(\rho E)) = \nabla\left(k\nabla T - \rho C\vec{V}T'\right) \quad (6)$$

ANSYS Fluent offers a range of upwind schemes, including power law, QUICK, second-order upwind, and first-order upwind. The governing equations were discretized with a finite volume method established by Patankar, utilizing the rapid distinction arrangement and decoupled via the SIMPLE process. The SIMPLE algorithm ensures mass conservation and determines the pressure field by connecting velocity and pressure corrections. Figure 3 illustrates the detailed steps of the SIMPLE technique. The critical variables (velocities, temperatures, pressures, and wall heat flows) were ascertained by iteratively solving the equations for momentum, mass, and energy until convergence was achieved. The solution was derived utilizing a second-order discretization method and a double-precision pressure-based solver.

Figure 4 illustrates that the energy equation has convergence residuals established at 10^{-6}, but the continuity, velocity, turbulence dissipation, and k equations each have convergence residuals set at 10^{-5}.

5.4 Turbulence models

A recent survey demonstrates that SAHs show improved thermo-hydraulic efficiency when functioning within Re ranging from 3000 to 19,000. The Re in the rectangular duct of the SAH demonstrates the presence of turbulent flow. The choice of a suitable turbulence design poses a considerable challenge in the design of an SAH using the CFD methodology. In the context of CFD simulations for flow through an SAH, it is essential to evaluate the precision of the simulation in depicting the actual flow dynamics. The question is intricate; the standard of the leading to output depends on various parameters of the computer approach. Modern computational fluid dynamics (CFD) software offers users a wide array of parameters for the mathematical model. The availability of various turbulence models raises the question of which model is most suitable for an SAH system. A turbulence design serves as a computational approach designed to resolve the system of mean flow equations. Turbulence models enable the calculation of mean flow without the need for an initial determination of the entire time-dependent flow field. Modern computational fluid dynamics (CFD) software offers a variety of techniques and models specifically designed for turbulence simulation. The approaches include [45]:

Reynolds-averaged simulation (RAS)/Reynolds-averaged The Navier-Stokes equations (RANS) are resolved in an ensemble-averaged format, using suitable models to account for turbulence effects.

Large eddy simulation (LES) involves formulas that govern the resolution of large turbulent structures in the flow, with the aim of analyzing the effects of subgrid scales (SGS). A filter is applied to the governing equations to achieve scale separation. The application of this filter influences the structural integrity of the SGS models throughout the process.

Detached Eddy Simulation (DES): A hybrid methodology that employs a Reynolds-averaged simulation (RAS) approach for near-wall regions and a Large Eddy Simulation (LES) approach for the bulk flow.

Direct numerical simulation (DNS) resolves all turbulence scales by mathematically solving the Navier-Stokes formulas without employing turbulence modeling.

AnSYS FLUENT 18.0, the commercial iteration of their computational fluid dynamics (CFD) program, includes a diverse array of turbulence models. AnSYS FLUENT 18.0 is employed to assess the turbulence models. The models comprise standard k-ε, realizable k-ε, renormalization-group RNG k-ε, standard k-ω, and shear stress transport (SST) k-ω. All of these models are evaluated.

5.5 Standard k-ε model

Two significant differences exist between the ordinary k-ε model and the realizable k-ε model [36], which are as follows:

- The realizable k-ε model presents an alternative formulation among the different approaches for turbulent viscosity.
- A modified transport equation has been derived from an exact equation that describes the transport of the mean-square vorticity fluctuation. The dissipation rate, represented by ε, has been calculated using this equation. The term "realizable" indicates that the model adheres to specific mathematical constraints related to the Reynolds stresses, consistent with the principles governing turbulent flows. Neither the RNG k-ε model nor the regular k-ε model do not satisfy the criterion of realizability. The obtainable and RNG k-ε models demonstrate significant enhancements over the conventional k-ε model in scenarios marked by considerable streamline curvature, vortex formation, and rotational effects. The model's relative novelty limits the understanding of specific situations in which the realizable k-ε model consistently outperforms the RNG model. Preliminary research indicates that the realizable model outperforms all variants of the k-ε model across various validations involving separated flows and flows with notable secondary flow characteristics. The formulation of the dissipation rate equation (ε) reveals a limitation in the conventional k-ε model and other classic k-ε models. The modeled dissipation equation is primarily accountable for the round-jet anomaly, characterized by precise predictions of spreading rates in planar jets, in contrast to inadequate predictions for axisymmetric jets.

5.7 Renormalization-group RNG k-ε

The RNG k-ε model was derived using a statistical method called renormalization group theory. Structurally, it resembles the traditional k-ε model, although it has the following modifications:

- The RNG model includes an additional component in its equation that improves accuracy for rapidly strained flows.
- The RNG model integrates the effects of swirl on turbulence, thereby enhancing accuracy for swirling flows.
- The RNG theory provides an analytical equation for turbulent Prandtl numbers, in contrast to the conventional k-ε model, which employs user-defined, fixed values.
- The traditional k-ε model is tailored for high Re conditions, whereas the RNG theory provides an analytically derived differential equation for effective viscosity that accounts for low Re effects. The effective use of this feature depends on the appropriate management of the near-wall zone.

The RNG k-ε model demonstrates enhanced accuracy and reliability across a wider spectrum of flow scenarios when compared to the conventional k-ε model, attributable to its distinct characteristics. The k-ε turbulence model based on RNG is developed through a mathematical framework referred to as "renormalization group" (RNG) methods applied to the instantaneous Navier-Stokes equations. The model incorporating various constants and supplementary terms and functions in the transport equations for k and ε is derived analytically, as opposed to the conventional k-ε model. A comprehensive explanation of RNG theory and its application to turbulence can be found by Jia et al. [36].

In the domain of fluid dynamics, such as the RNG k-ε model, we simulate the behavior of turbulence continuously. With equations that elucidate the exuberance of kinetic energy and the clarity of its dissipation rate. These equations are utilized in the renormalization group. In the k-ε paradigm, they interact and engage, facilitating our comprehension in an astute manner.

$$\frac{\partial}{\partial x_j}(\rho\kappa u_j)=\frac{\partial}{\partial x_j}\left[\sigma_\kappa\mu_{eff}\frac{\partial\kappa}{\partial x_j}\right]+G_\kappa+G_b-\rho\varepsilon \tag{7}$$

$$\frac{\partial}{\partial x_j}(\rho\varepsilon u_j)=\frac{\partial}{\partial x_j}\left[\sigma_\varepsilon\mu_{eff}\frac{\partial\varepsilon}{\partial x_j}\right]+G_{1\varepsilon}\frac{\varepsilon}{\kappa}(G_\kappa+G_{3\varepsilon}G_b)-C_{2\varepsilon}\rho\frac{\varepsilon}{\kappa}-R_\varepsilon \tag{8}$$

where,
G_k: This stands for the k-generation caused by the mean velocity gradients.
G_b: This denotes the formation of k due to buoyancy.

The inverse effective Prandtl numbers for k and ε are represented by α_k and α_ε, respectively. α_k=α_ε=1.393.

The primary distinction between the RNG and ordinary k-ε models is the supplementary term in the ε equation expressed as follows:

$$R_\varepsilon=\frac{C_\mu\rho\eta^3(1-\eta/\eta_0)}{1+\beta\eta^2}\frac{\varepsilon^2}{\kappa} \tag{9}$$

where, η=(k/ε), η_0=4.38, β=0.012.

The next parameters present a list of constants utilized in the model.

$G_{1\varepsilon}$=1.42, $C_{2\varepsilon}$=1.68, $C_{3\varepsilon}$=1.8, C_μ=0.0845.

5.8 Standard k-ω

The ANSYS Fluent standard k-ε model is derived from the Wilcox k-ε model [36], which has been revised to incorporate shear flow dispersion, compressibility, and the effects of low Re. The sensitivity of the solutions to values of k and ϋ beyond the shear layer, referred to as freestream sensitivity, constitutes a limitation of the Wilcox model. The influence on the solution can be significant, especially for free shear flows, despite the updated formulation in ANSYS Fluent having alleviated this dependence [35].

- The blending function multiplies the standard k-ϋ model with the modified k-ε model, subsequently integrating the two models.
- To activate the standard k-ϋ model, the blending function is assigned a value of one in the near-wall region and zero in areas away from the surface. This enables the operation of the converted k-ε model.
- The SST model incorporates a damped cross-diffusion derivative term in the ϋ equation.
- The transport of turbulent shear stress is addressed through an adjustment of the concept of turbulent viscosity.
- A discrepancy exists in the modeling constants.

The SST k-ω model exhibits enhanced accuracy and reliability across a broader range of flow scenarios compared to the standard k-ω model [34].

5.9 Boundary conditions

The simulation was conducted under the following boundary conditions such as:

▪ In the inlet section, a mass flow rate (MSR) limitation of 0.01 to 0.05 kg/s is associated with Res between 3000 and 10000, with an inlet temperature of T_{inlet} =300.15 K (look at Table 1). Table 2 presents the thermal and physical characteristics of the air and absorber plate. It is expected that these factors will stay consistent at the typical bulk temperature outlined subsequently. These features are presented as they are, with no alterations.

Table 1. Conditions at the boundaries for application of the model

	BC1	BC2	BC3	BC4	BC5
Mass flow rate (kg/s)	0.01	0.02	0.03	0.04	0.05
Absorber heat flux	The value is specified according to the month, Day, and time of the day	The value is specified according to the month, Day, and time of the day	The value is specified according to the month, Day, and time of the day	The value is specified according to the month, Day, and time of the day	The value is specified according to the month, Day, and time of the day
Backside and side borders of heat flux (HF)	Adiabatic process Q= 0		Backside and side borders of heat flux (HF)	Adiabatic process Q= 0	

Table 2. Conditions for computational fluid dynamics (CFD) studies involving air and absorber plates

Features	Fluid (Air)	Absorptivity of the Panel (Aluminum)
Density, 'ρ' [kg/m^3]	1.167	2719
Viscosity, 'μ' [kg/ms]	1.85 e-05	---
Thermal conductivity, 'λ'[W/mK]	0.0262	202.4
Specific heat, 'Cp' [J/kgK]	1006	871

6. VALIDATION OF THE NUMERICAL MODEL

6.1 Grid sensitive analysis

A mesh independence test was performed for the scenario of Re=3000 by evaluating five different cell counts to reduce the impact based on the findings of the computational analysis concerning outlet air temperature. The outcomes of the mesh independence test are displayed in Table 3. The implementation of the solutions entailed a significant increase in the number of cells, rising from 771,023 to 4,857,325. A total of 4,524,939 cells were chosen, derived from the minimal percentage variation of the *Tout*.

Table 3. Testing the grid independence

Cells Number	Tout (K)	Percentage Deviation of Tout (%)
771023	55.75	
1102031	56.17	0.123
1524097	56.95	0.428
4524939	58.92	0.575
4857325	60.05	0.328

6.2 Turbulence models validation

Roughened gutters were utilized to improve HT by elevating the turbulence level in the fluid flow. Besides, an evaluation was carried out to evaluate the appropriateness of various turbulence patterns concerning the introduced numerical issue, thus guaranteeing the accuracy of the numerical results. This assessment employed five recognized classical turbulence configurations: Standard k-ε, RNG k-ε, realizable k-ε, and k-ω models. The preciseness of the adopted configurations was assessed by comparing its outcomes with data from existing previous work. The values of the Nusselt number (*Nu*) and friction factor (*f*) were obtained from a numerical configuration that employs various turbulence configurations. The values were subsequently compared to the standard correlations set forth by Dittus-Boelter [34] (Eq. (10)) and Modified Blasius [46] (Eq. (11)).

$$Nu= 0.023Re^{0.8}Pr^{0.4} \tag{10}$$

$$f= 0.791Re^{-0.25} \tag{11}$$

The numerical simulations of *Nu* and *f* were validated using Eqs. (10) and (11) for Res ranging from 3000 to 10000. Figures 5 and 6 present a comparison of the predicted and calculated (via correlation) Nu and *f* values. The analysis demonstrates the most precise representation of the RNG k-ε configurations. The *Nu* and *f* estimated by the RNG k-ε configurations exhibit typical percentage deviations of ±11.8% and ±5.9%, respectively, when compared to values obtained from the previously mentioned correlations within the same Re range. Additionally, Tables 4 and 5 present the deviations of all configurations for each data point. The RNG k-ε turbulence configurations have been employed in prior numerical research related to roughened SAHs, as indicated in references [34-39]. The RNG k-ε configurations have been adopted for this computational fluid dynamics analysis.

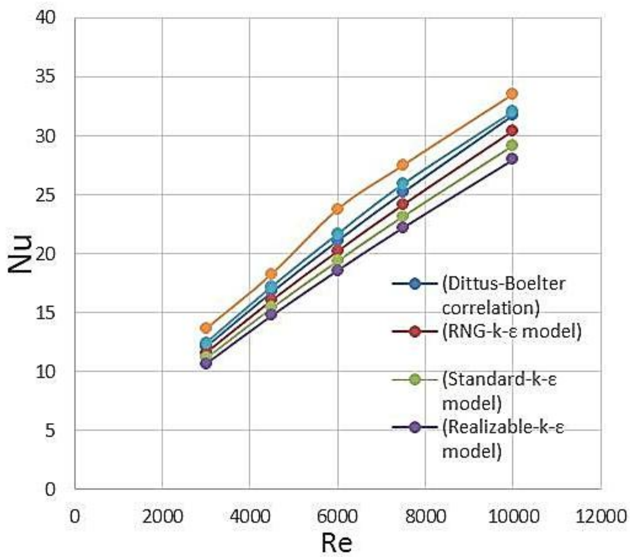

Figure 5. Examining the expected *Nu* values using Dittus-Boelter correlations across various turbulence configurations [30]

Table 4. Nusselt number deviation

RNG-k-ε Configurations	Standard-k-ε Configurations	Realizable-k-ε Configurations	Standard-k-ω Configurations	SST-k-ω Configurations
5.9%	8.1%	7.3%	6.6%	9.0%
8.9%	12.2%	10.9%	9.8%	13.5%
11.8%	16.2%	14.6%	13.1%	18.0%
14.8%	20.3%	18.2%	16.4%	22.5%
17.7%	24.3%	21.9%	19.7%	27.0%

Table 5. Friction factor deviation

RNG-k-ε Configurations	Standard-k-ε Configurations	Realizable-k-ε Configurations	Standard-k-ω Configurations	SST-k-ω Configurations
3.5%	3.9%	4.4%	5.4%	4.9%
4.7%	5.2%	5.8%	7.2%	6.5%
5.9%	6.6%	7.3%	9.0%	8.1%
7.1%	7.9%	8.7%	10.8%	9.7%
8.3%	9.2%	10.2%	12.6%	11.3%

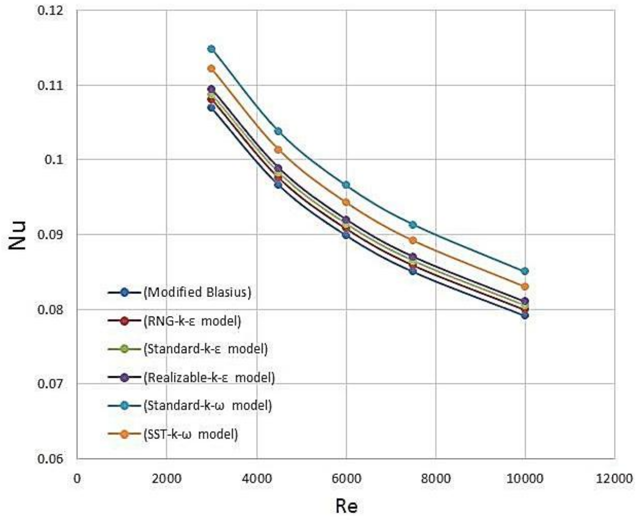

Figure 6. Analysis of predicted *f* values across various turbulence configurations in relation to the Modified Blasius correlation [42]

7. RESULTS AND DISCUSSION

7.1 Effect of experiment day on solar radiation

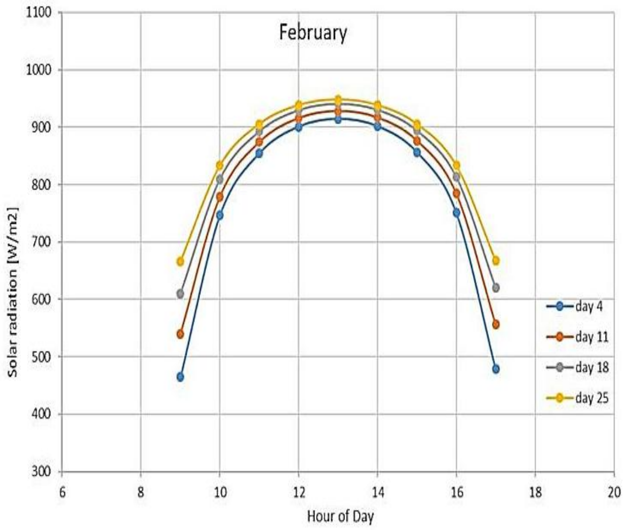

Figure 7. Variation of solar radiation along the hour of the day in February month for four days only for configurations-1 of SAH at Re=3000

The main goal of the SAH is to increase the air temperature for applications in industry and for heating in residential settings. Figures 7, 8, 9, and 10 depict the progression of average solar radiation practically measured across the hours of the day in February, March, April, and May for the full-duct configurations of the SAH. The findings show that solar intensity increases steadily from the start of the morning, reaching its maximum around 13:00, then decreasing for the rest of the day until the end of the experimental observations. The profile shows that solar intensity remains largely uniform throughout the experimental days due to reliable solar tracking mechanisms. The figures demonstrate that the maximum variation in solar intensity across the four days is roughly 5.5%. This suggests that assessing outcomes on various days does not notably influence the results obtained. The findings reveal a steady pattern in solar intensity, rising progressively until around 12:30 PM, after which there is a decrease leading to the end of the experimental testing phase. The observed time lag in maximum solar intensity may be attributed to the time needed to warm the SAHs and the ambient air around them. The results show that the solar intensity surpasses the temperature of the glass cover, and it is also higher than the outlet air temperature as a result of HT from the absorber plate to the air. The results revealed that approximately 948.2, 950.4, 939.4, and 900.4 W/m^2 correspond to the maximum solar intensity at about 13:00 am in February, March, April, and May, respectively. The results indicated that the solar intensity has a maximum in February and a minimum value in May, and this leads to increasing the benefit of heating capacity in February and March in practical use.

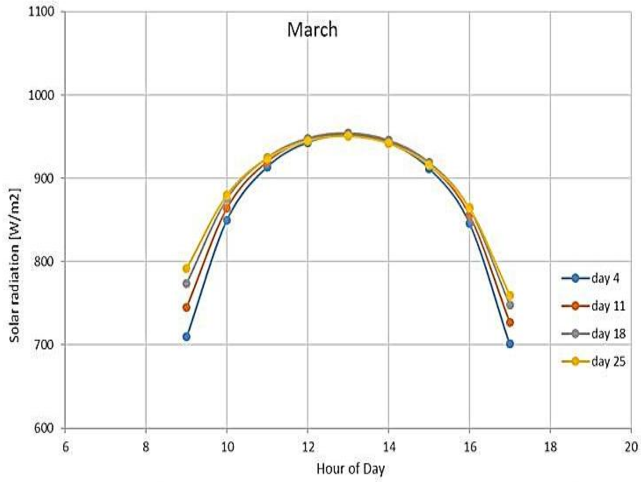

Figure 8. Variation of solar radiation along the hour of the day in March for four days only for configurations-1 of SAH at Re=3000

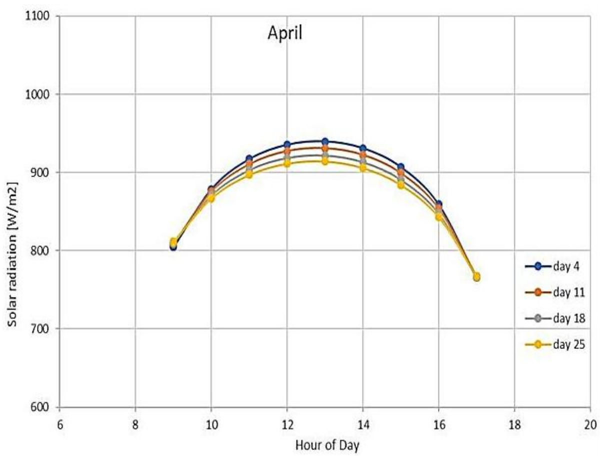

Figure 9. Variation of solar radiation along the hour of the day in April month for four days only for configurations-1 of SAH at Re=3000

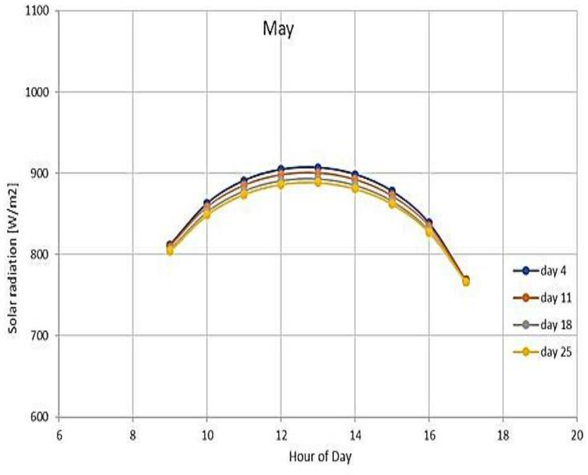

Figure 10. Variation of solar radiation along the hour of the day in May month for four days only for configurations-1 of SAH at Re=3000

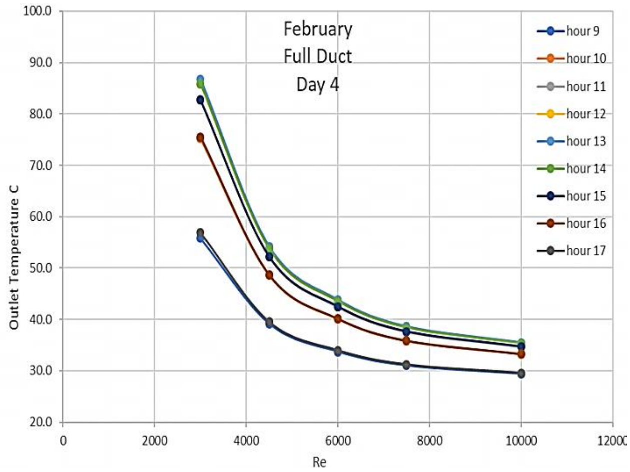

Figure 11. Variation of the outlet temperatures with Re on 4 Feb. 2024 for various hours in the day

7.2 Effect of experiment day on the outlet air temperature

However, the outlet air temperature from the SAH in the case of full-duct configurations of SAH for four months of testing in February, March, April, and May, respectively, is illustrated in Figures 11 to 18. The outlet temperatures for the two days are 4 and 25 for hours from 9 to 17 during the day. The maximum outlet air temperatures SAH are located at 12:00, 13:00, and 14:00 for various Res. The graphical curve representations suggested that the peak outlet air temperature achieved at a low Reynolds number of Re = 3000 was attributable to a reduction in the duration of the hot air flow and an augmentation of the heat transfer rate throughout the diurnal cycle. Furthermore, considering that it constitutes half of the total peripheral area of the absorber, the tubular solar air heater exhibits a more extensive surface area exposed to solar irradiation in comparison to the conventional solar air heater. Also, as we'll see in a little, the SAH absorber structure reduces top heat loss by reducing reflected solar radiation to the environment via internal reflections between the absorber tubes' surfaces. What this means is that compared to SAH, the HT to the air is significantly higher. It is noted that, for example, at a Re=3000, the maximum outlet temperatures are 86.74, 73.3, 68.52, 63.72, and 59.26°C at Re=3000 at 13:00 am on day 4 February for full duct, first half duct, middle half duct, end half duct, and empty duct. Also, in Figure 11 and Figure 12, the maximum outlet temperatures are 89.1, 75.6, 70.34, 65.42, and 60.84°C at Re=3000 at 13:00 am on 25 February for full duct, first half duct, middle half duct, end half duct, and empty duct. Also, as presented in the numerical results, the maximum outlet temperatures at day 4 in the February month are 85.68°C in March and 85.68°C in March.

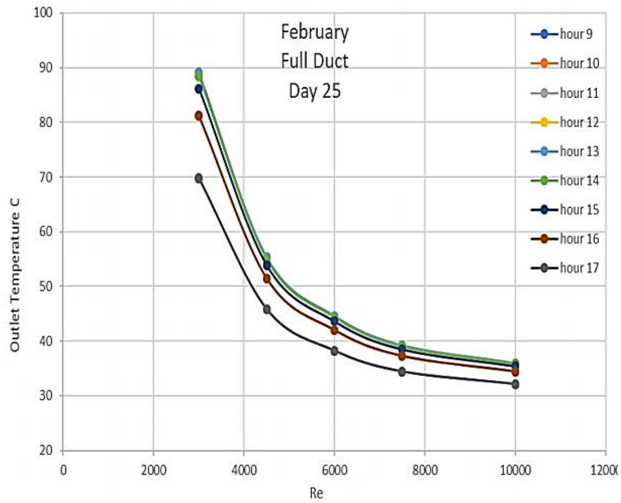

Figure 12. Variation of the outlet temperatures with Re on 25 Feb. 2024 for various hours in the day

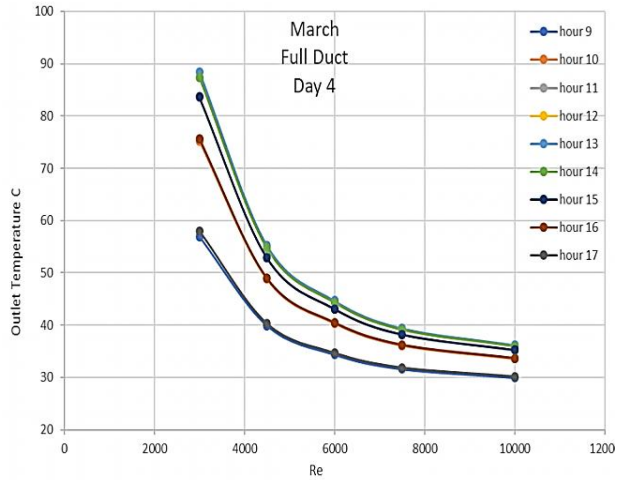

Figure 13. Variation of the outlet temperatures with Re on 4 Mar. 2024 for various hours in the day

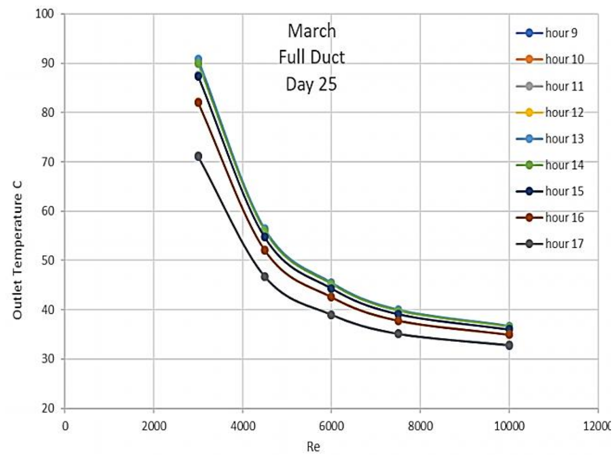

Figure 14. Variation of the outlet temperatures with Re on 25 Mar. 2024 for various hours in the day

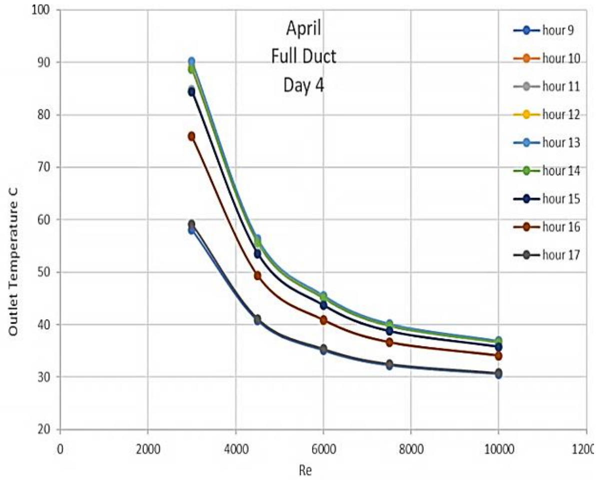

Figure 15. Variation of the outlet temperatures with Re on 4 Apr. 2024 for various hours in the day for configurations-1 air solar heater

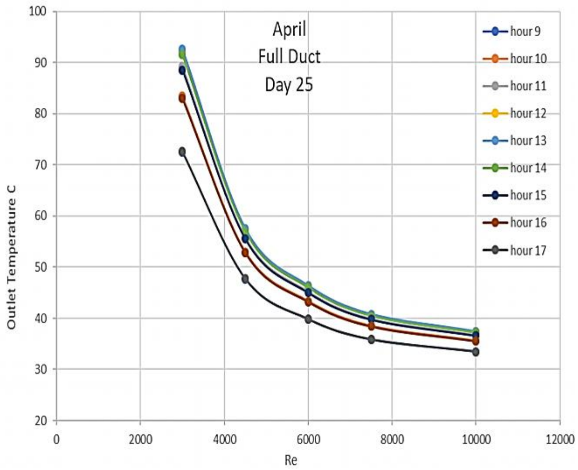

Figure 16. Variation of the outlet temperatures with Re on 25 Apr. 2024 for various hours in the day for configurations-1 air solar heater

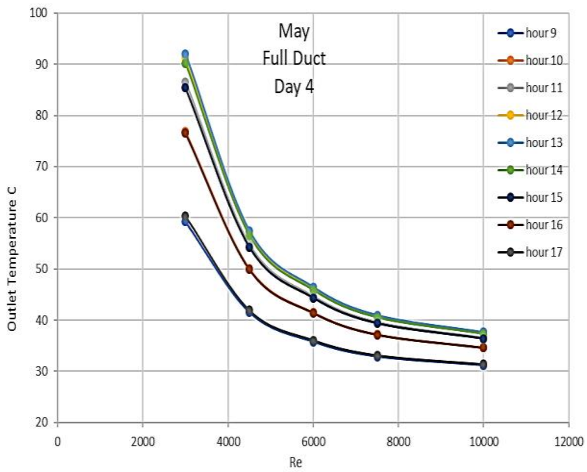

Figure 17. Variation of the outlet temperatures with Re on 4 May 2024 for various hours in the day for configurations-1 air solar heater

7.3 Effect of duct type on outlet air temperature

The main goal of the present study is the investigation of the influence of using various types of SAH that are plotted in Figures 19 to 22. The numerical results were plotted for two days of 4 and 25 from the four months of February, March, April, and May at the highest time of 13:00 am. The results showed that the maximum outlet temperatures are 86.74, 73.3, 68.52, 63.72, 59.26°C for full duct, first half duct, middle half duct, end half duct, and empty duct, respectively, at Re=3000 at 13:00 am on day 4 February. Also, the maximum outlet temperatures are 89.1, 75.6, 70.34, 65.42, and 60.84°C for full duct, first half duct, middle half duct, end half duct, and empty duct, respectively, at Re=3000 at 13:00 am on day 25 February. Thus, we can decide that the full duct configuration is the best configuration due to the increase in the outlet temperatures as compared with the other configurations; also, the worst configuration was the empty duct due to the lowest outlet temperatures. The effect of the Re is seen from these figures that, for the same length of collector plate, if the flow rate increases, then the outlet air temperature decreases for all configurations and the two days of the experiment, i.e. the output from the solar cells increases for all the cases of the area covered by solar cells. This is true in both winter and summer conditions. For example, in Figure 13, the maximum outlet temperatures were as follows: about 85.86, 52.23, 42.51, 35.86, 34.70°C at 13:00 am day 4 February for Re=3000, 4500, 6000, 7000, and 10000 respectively. But in Figure 14, the maximum outlet temperatures were as follows: about 88.44, 53.89, 43.64, 38.49, 34.42°C at 13:00 am on day 25 February for 3000, 4500, 6000, 7000, and 10000, respectively.

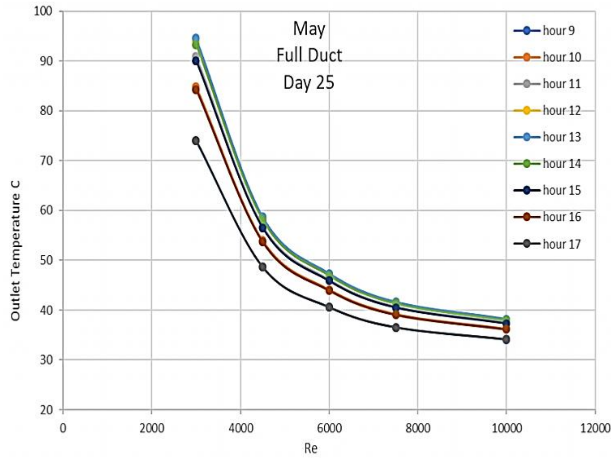

Figure 18. Variation of the outlet temperatures with Re on 25 May 2024 for various hours in the day for configurations-1 air solar heater

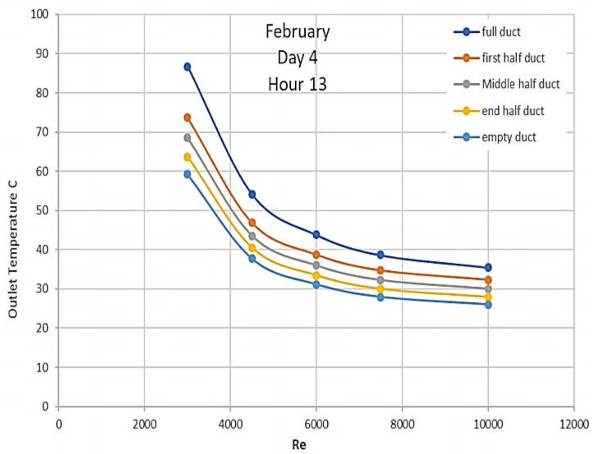

Figure 19. Relationship between the outlet temperatures with Re at hour 13 on 4 Feb. 2024 month for various configurations of the SAH

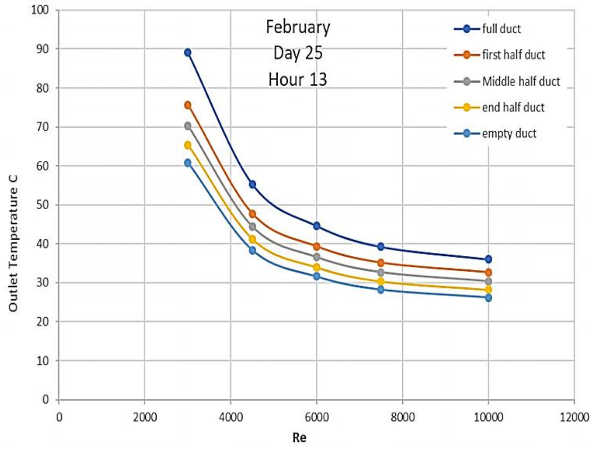

Figure 20. Relationship between the outlet temperatures with Re at hour 13 on 25 Feb. 2024 month for various configurations of the SAH

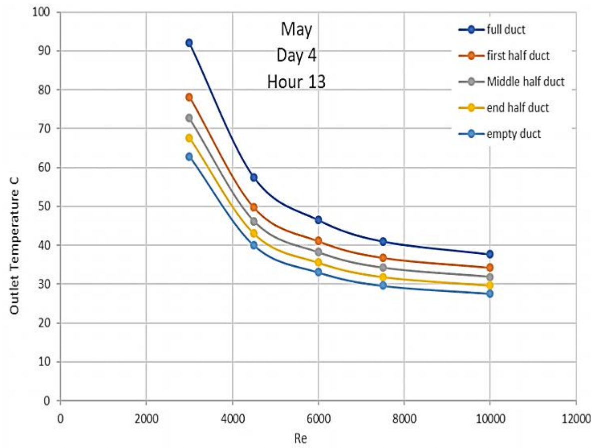

Figure 21. Relationship between the outlet temperatures with Re at hour 13 on 4 May 2024 for various configurations of the SAH

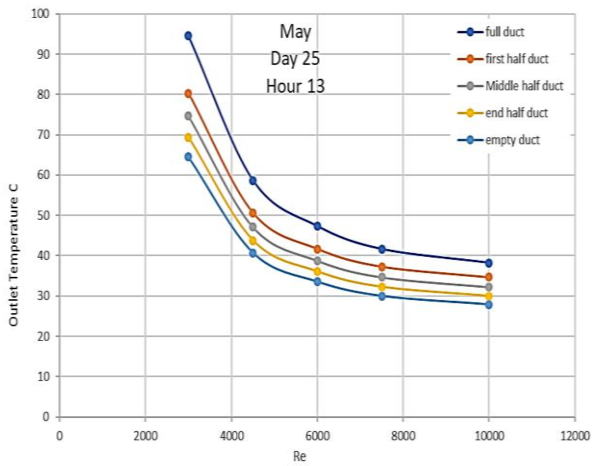

Figure 22. Relationship between the outlet temperatures with Re at hour 13 on 25 May 2024 for various configurations of the SAH

7.4 Effect of duct type on Nusselt number (*Nu)*

An analysis was conducted on the elements meeting the criteria for high-performance roughness surface geometries, and their performance was compared under identical operating conditions. The variation of the *Nu* with respect to the Re is observed for different roughness geometries employed in SAH ducts, specifically between the values of 23 and 30 (Figures 23-30). The categories comprise full ducts, first half ducts, middle half ducts, end half ducts, and empty ducts. Measurements were conducted at Re=3000 at 13:00 on four days in February, twenty-five days in March, and twenty-five days in April and May. The *Nu* is consistently higher for an SAH featuring artificial roughness compared to one lacking it. The rib's capacity to generate secondary flow enhances HT performance through the implementation of artificial roughness. The central core region of the SAH facilitates the transport of cold fluid to the ribbed absorbed surface through a secondary flow characterized by two counter-rotating vortices. The interactions of these cells with the primary flow disrupt the development of the boundary layer downstream of the reattachment areas, thereby influencing recirculation and flow reattachment between the ribs. The *Nu* for the roughened duct relative to the smooth duct consistently increases with the Re, as illustrated in this figure. With an increase in the Re, there is a corresponding increase in velocity, resulting in an enhanced rate of HT. Roughness elements begin to extend beyond the laminar sub-layer as the Re increases. A Reynolds number Re is associated with a decrease in the thickness of the laminar sub-layer. Furthermore, the vortices that arise from the roughness elements play a significant role in localized heat dissipation. The heat transfer rate is enhanced as a result of this phenomenon when juxtaposed with a smooth surface. On February 4, the *Nu* enhancements for the entire duct, first half of the duct, middle half of the duct, and end half of the duct were 59%, 54%, 50%, and 29%, respectively, in comparison to the empty duct.

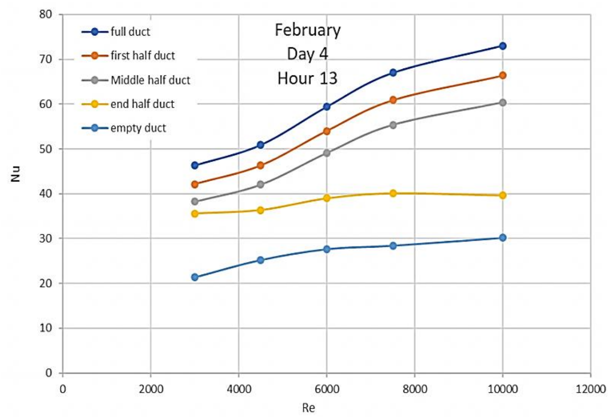

Figure 23. Variation of the *Nu* with Re at hour 13 on 4 Feb. 2024 for various configurations of the SAH

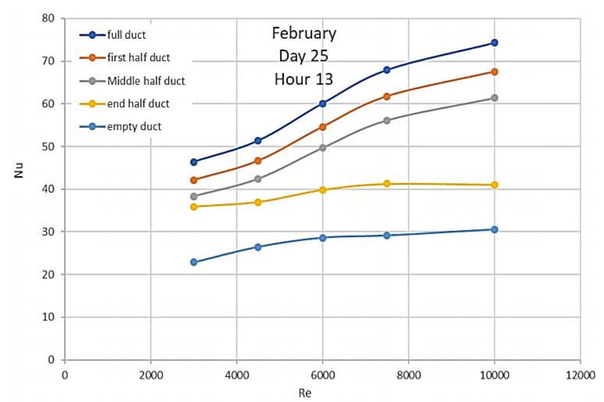

Figure 24. Variation of the *Nu* with Re at hour 13 on 25 Feb. 2024 for various configurations of the SAH

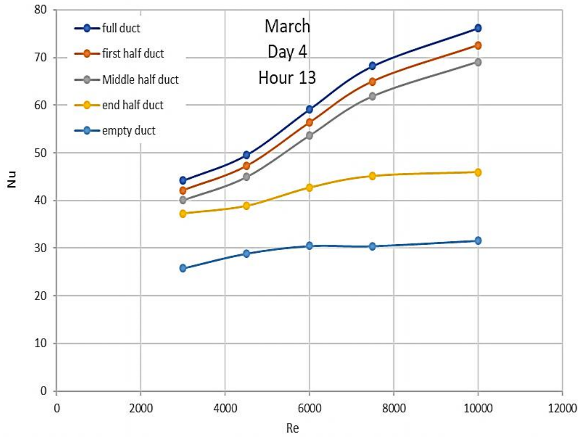

Figure 25. Variation of the *Nu* with Re at hour 13 on 4 Mar. 2024 for various configurations of the SAH

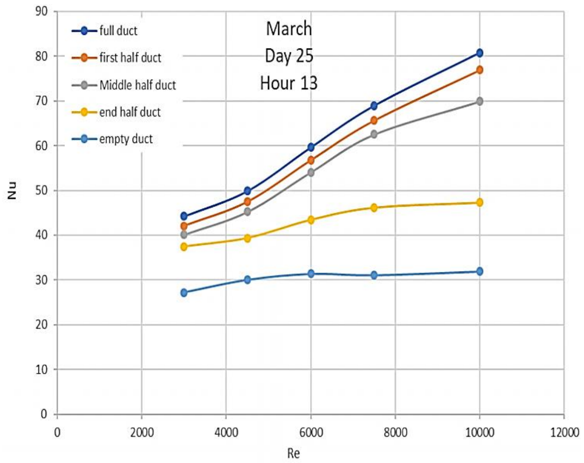

Figure 26. Variation of the *Nu* with Re at hour 13 on 25 Mar. 2024 for various configurations of the SAH

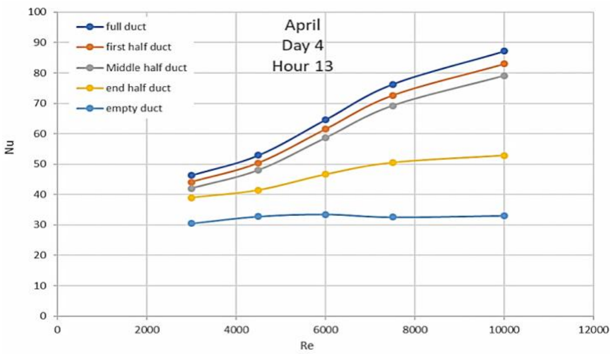

Figure 27. Variation of the *Nu* with Re at hour 13 on 4 Apr. 2024 for various configurations of the SAH

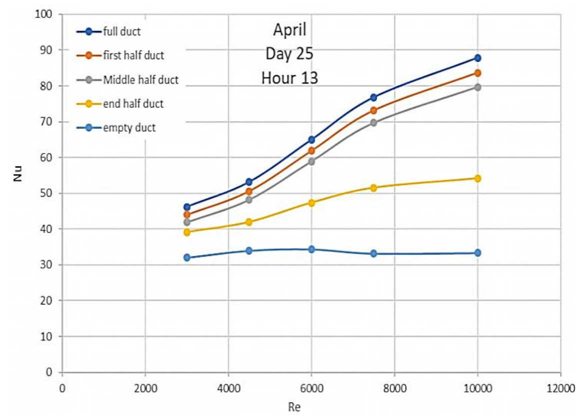

Figure 28. Variation of the *Nu* with Re at hour 13 on 25 Apr. 2024 for various configurations of the SAH

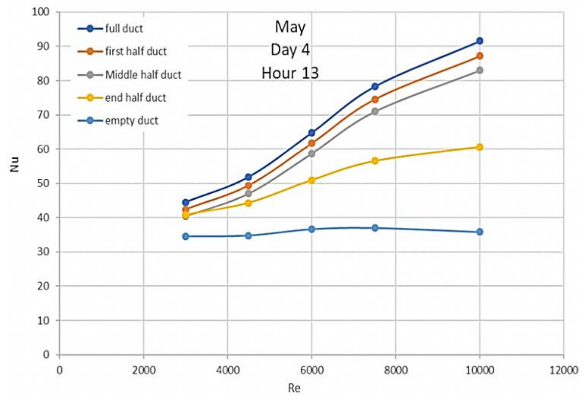

Figure 29. Variation of the *Nu* with Re at hour 13 on 4 Apr. 2024 for various configurations of the SAH

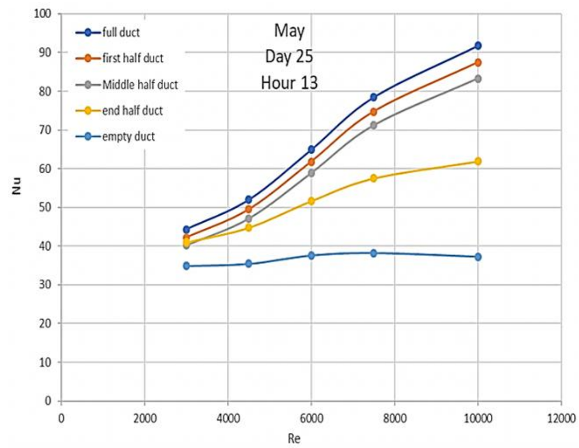

Figure 30. Variation of the *Nu* with Re at hour 13 on 25 Apr. 2024 for various configurations of the SAH

7.5 Effect of Re on *Nu*

The effect of Re and the day hours on the HT and *Nu* are clearly depicted in Figures 31 to 34. In these figures, the changing of *Nu* with Re is given for full duct at 13:00 am for 4 and 25 days in February, March, April, and May at the highest temperatures time of 13:00 am of the day. The heat acquired is directly proportional to the efficiency of the collector, as established. The identified critical factors for collector efficiency are ambient air temperature, the total heat loss coefficient of the collector, and the efficiency factor of the collector. Therefore, it would be more pragmatic to compare the HT of the collectors with the correlations. For a fully developed turbulent airflow between two insulated plates, one of which is thermally energized. According to this equation obtained for turbulent flow, *Nu* changed for $3000 < Re < 10000$. The results indicated that the full-duct rough flat plate and absorber configurations exhibited the highest *Nu* relative to the other configurations. The convective heat coefficient may decrease as a result of reduced usable heat gain (Q) and an increased logarithmic mean temperature differential. The *Nu* for HT, which correlates positively with the Re, remained positive throughout the day. Two potential explanations include, first, flows resulting from the formation of swirls as the flow line extends, and second, flows arising from the staggering of the flow line in relation to surface geometry. The introduction of turbulence to the fluid increased the *Nu* and the convective HT coefficient. As a result, the *Nu* increased by 34%, 30%, 25%, 18%, and 11% for 3000, 4500, 6000, 7000, and 10000, respectively, for hour 14 of day 4 February. As shown in the figures, the *Nu* increases to the maximum highest number at 14:00 and 13:00 in the day, and the maximum *Nu* is located at high Re=10000 and the minimum *Nu* at Re=3000.

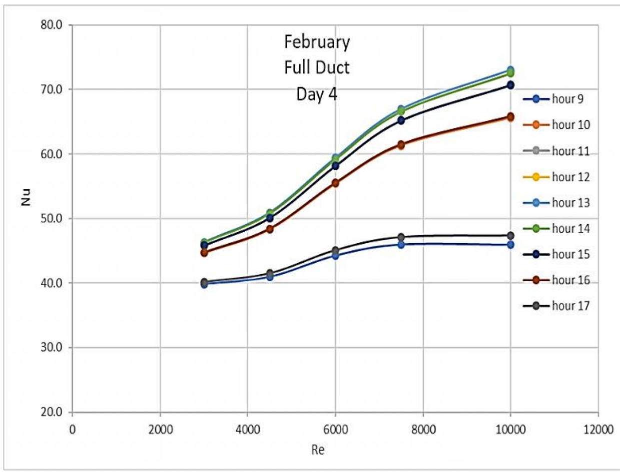

Figure 31. Variation of the *Nu* with Re on 4 Feb. 2024 for various hours in the day for configurations-1 air solar heater

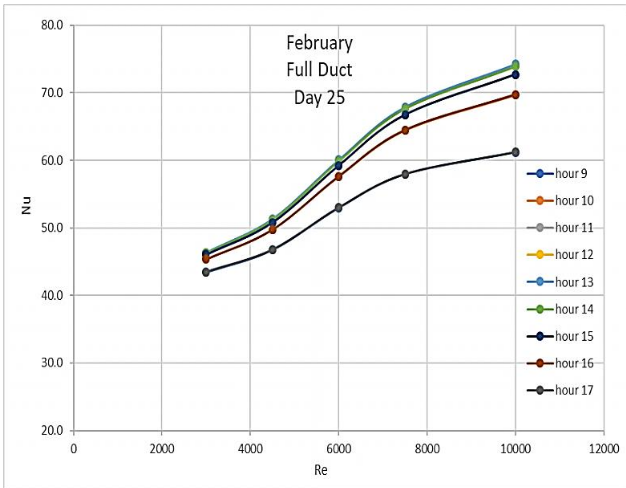

Figure 32. Variation of the *Nu* with Re on 25 Feb. 2024 for various hours in the day for configurations-1 air solar heater

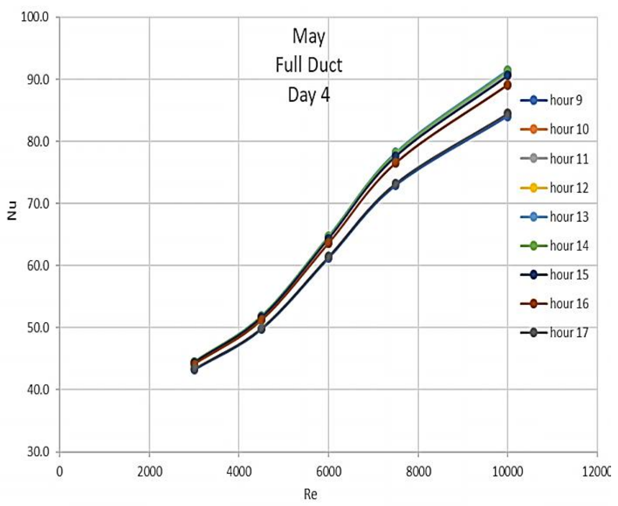

Figure 33. Variation of the *Nu* with Re on 4 May 2024 for various hours in the day for configurations-1 air solar heater

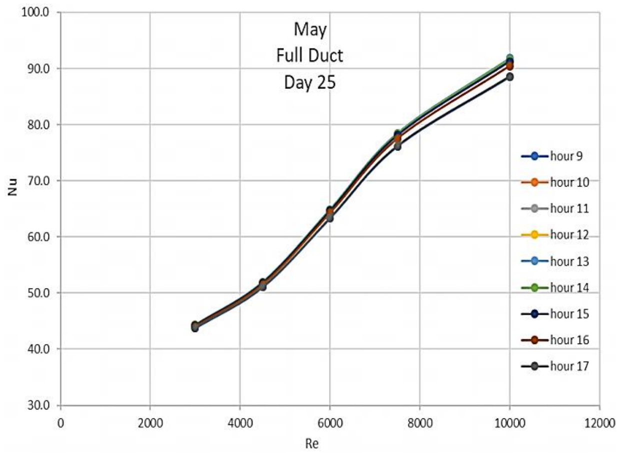

Figure 34. Variation of the *Nu* with Re on 25 May 2024 for various hours in the day for configurations-1 air solar heater

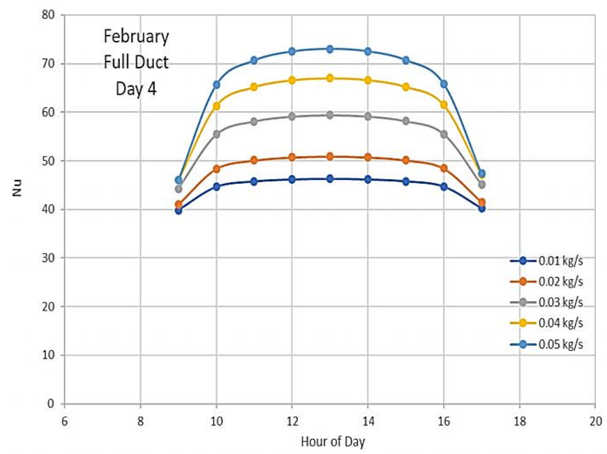

Figure 35. Variation of the *Nu* with hours of the day on 4 Feb. 2024 for various MSRs for configurations-1 air solar heater

7.6 Effect of mass flowrate on *Nu*

The effect of MSR and the day hours on the HT and *Nu* are plotted in Figures 35 to 36. The increase of *Nu* with Re is given for full duct at 13:00 am for 4 and 25 days in February, March, April, and May, respectively. The highest *Nu* occurred at the height temperature at mid of the day at 12:00, 13:00, and 14:00 am. The primary parameters influencing collector efficiency are ambient air temperature, the total heat loss coefficient of the collector, and the efficiency factor of the collector. Thus, a more realistic approach would involve comparing the HT of the collectors with the established correlations. In a fully developed turbulent flow of air between two insulated plates, one plate is heated. The *Nu* exhibited variation for the range 3000 < Re < 10000, as determined by the equation formulated for turbulent flow. The results indicated that the full-duct rough flat plate and absorber configurations exhibited the highest *Nu* in comparison to the other configurations. The convective heat coefficient may decrease due to a reduced usable heat gain (Q) and an increased logarithmic mean temperature differential. An increased Re correlates with an elevated HT *Nu* at all times of the day. Two potential explanations exist: first, flows resulting from the formation of swirls as the flow line extends; second, flows arising from the staggering of the flow line in relation to surface geometry. By increasing the turbulence of the fluid, we were able to enhance both the Nu and the convective HT coefficient. As a result, the Nu increased by 73, 67, 59, 50, and 46 for mass flowrate of 0.01, 0.02, 0.03, 0.04, and 0.05 kg/sec, respectively, for the case of using full duct and 4 days of February month at 13:00 hour. As a result, the Nu increased by 76, 68, 59, 49, and 44 for mass flowrate of 0.01, 0.02, 0.03, 0.04, and 0.05 kg/sec respectively for cases of using full duct and 4 days of March month at 13:00 hour.

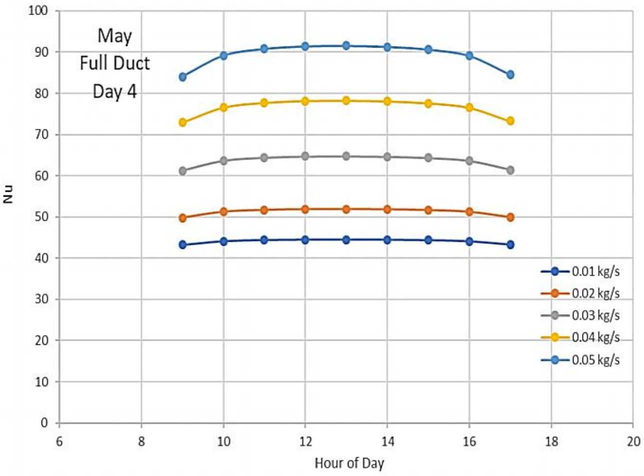

Figure 36. Variation of the Nu with hours of the day on 4 Apr. 2024 for various MSRs for configurations-1 air solar heater

7.7 Friction factor (f)

The fluctuation versus Re for each of the scenarios was displayed in Figure 37. The values in this context exhibit an inverse relationship, with the f decreasing as the Re increases. Furthermore, the graph indicates that the curves gradually approach a constant value from Re=4500 to Re=10000. In addition, case E yielded the highest f of 98%, with cases B, C, and D following closely with nearly similar friction factors (45% up, 42% down, and 39% middle, respectively). As far as the smooth channel is concerned, it has recorded the lowest value of f. The decrease is attributed to the fact that the position of the baffles interferes with the flow of the fluid, which in turn led to an increase in the pressure drop and f. Moreover, in comparison to the other examples, the maximum value of f was 0.08 at Re=3000, while Case E yielded a maximum value of 0.14; nonetheless, as the Re grew, the f decreased for all cases because the airflow rate increased and the friction drag decreased.

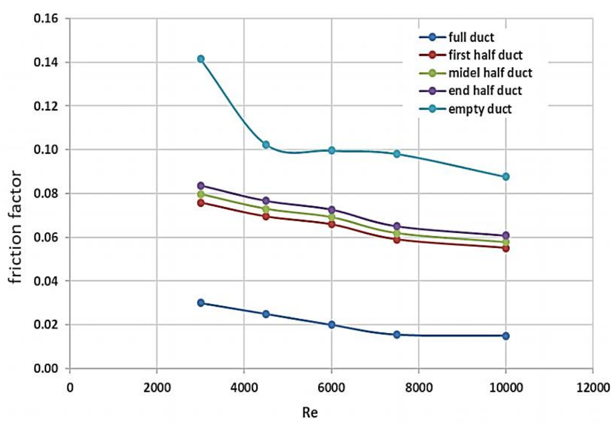

Figure 37. The friction factor is dependent on the Re across all scenarios

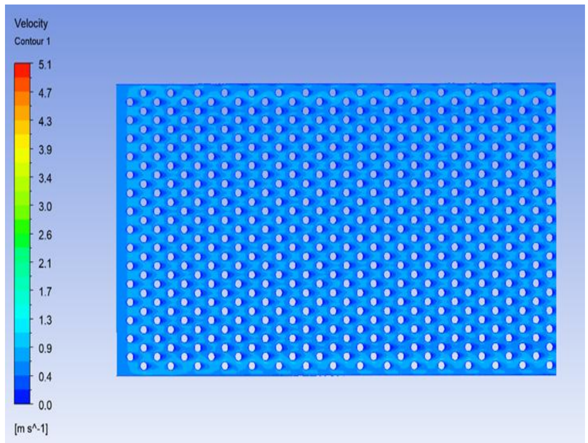

Re=3000

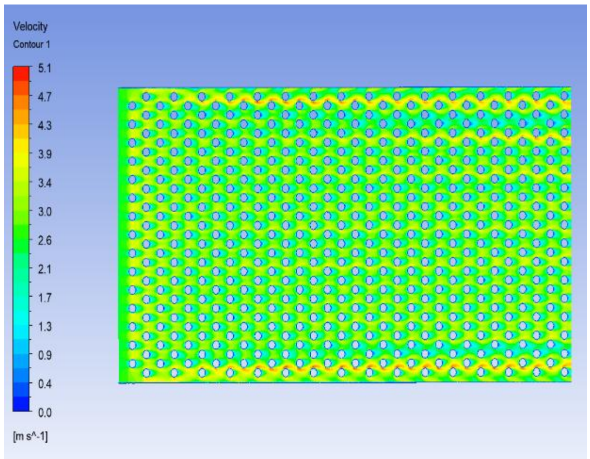

Re=10000

Figure 38. Contour of velocity distribution with Re on month of May day 25 at hour 13 for the full duct configurations air solar heater

7.8 Temperatures and velocity counters

To verify the results that were obtained by using the numerical part of the CFD configuration sing of the SAH, the thermal and aerodynamic characteristics of a smooth (unrouged) surface were compared with the other configurations of (roughed) absorber surface as the contour of temperature, velocity and pressure along the absorber of the SAH. Figure 38 shows the effect of Re for the data obtained by the CFD configurations described by using the velocity distribution near the absorber plate. The results showed that the maximum velocity separated in the region between the roughed sections in case of increasing the Re due to increasing the vorticity in the region between the fins due to decreasing the air flow rate. In general, the adequacy of the developed computer SAH configurations to a real SAH was shown: the behavior of the configurations quite accurately coincides with the behavior of the simulated object under the same simulation conditions, and the configurations are convincingly presented with respect to the SAH properties predicted by the configurations. The numerical study considers the average Res corresponding to the airflow in the SAH on the pressure distribution in the channel of the air heater. The results of the pressure are presented in Figure 39, which shows the effect of increasing the Re from 3000 to 10000 on the pressure distribution. The results illustrated that the pressure distribution will be affected by increasing the Re extremely by increasing the pressure at the entrance of the duct from 2.9 pa to 47.2 pa as the pressure increased from 3000 to 10000 due to increasing the flow rate of the air flow shown in Figure 40. The contour shows the distribution of air temperature in the channel cross-section of the air solar heater for the Re=3000 to 10000. The temperature distribution starts from the middle of the absorber plate from 47 to 82°C at Re=3000, but it starts from 37 to 45°C approximately at Re=10000 due to increasing the cooling effect by air caused by increasing the air flow rate and increasing the HT.

7.9 Effect of configuration types

The effect of using three configurations of the roughed duct that varied the location of the roughed surface by smooth roughed surface, right roughed surface, middle roughed surface, and left roughed surface and compared the effect with the smooth configurations and with the full roughed configurations that were discussed in the previous section. The contour showing the distribution of air temperature, velocity, and pressure in the channel cross-section for the Re=10000 was presented in Figures 41, 42, and 43, respectively. The nature of the vortices formed behind the first five fins located along the airflow is shown in the Figures. Due to a frontal airflow impact, a separate flow is formed behind the first region, which does not have a significant effect on the HT. Further on, the flow stabilizes, and stable vortices are formed in the inter financial region, full development of which occurs after the passage of the fourth fin. The presence of a rough right surface on the light-absorbing surface will lead to destroying the boundary layer, increasing the velocity, and increasing the temperature distribution. Therefore, an increase in the **k** is observed. A turbulence kinetic-energy contour obtained with the CFD configurations is shown in the Figures. The k is a turbulence force in the airflow field. The kinetic-energy contour makes it possible to understand the effect of the artificially created surface roughness on the intensity of heat exchange between the surface and air. The results showed that the maximum value of the kinetic energy is observed near the light-absorbing surface between the fins, and then it decreases with an increase in the distance from the surface. Thus, the presence of a rough surface significantly enhances heat exchange processes near the light-absorbing surface. On the Re for light-absorbing surfaces with different fin pitches obtained by the developed configurations for various Res 3000>Re>10000.

Finally, Table 6 shows the concluded Produced Correlations of the experimental results.

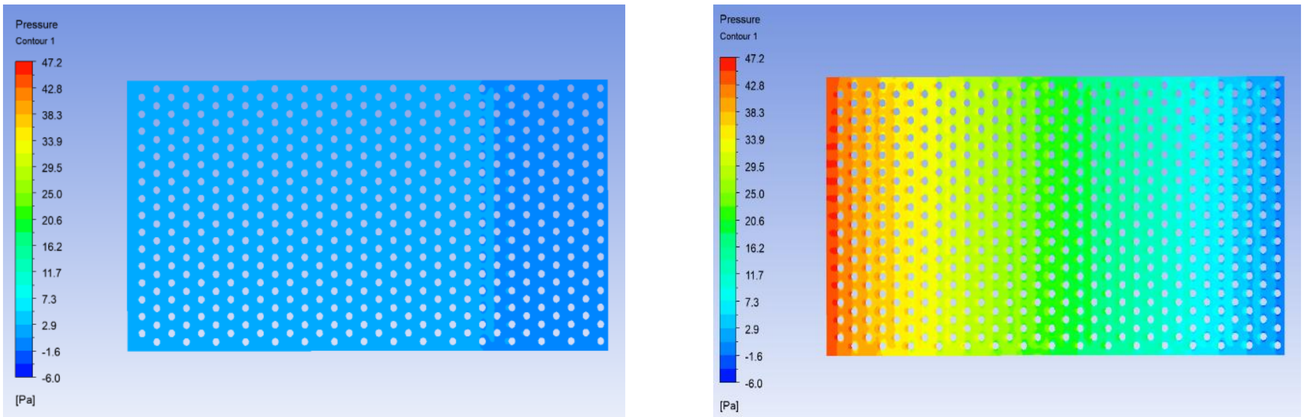

Re=3000 Re=10000

Figure 39. Contour of pressure distribution with Re on month of May 25 at hour 13 for the full duct configurations air solar heater

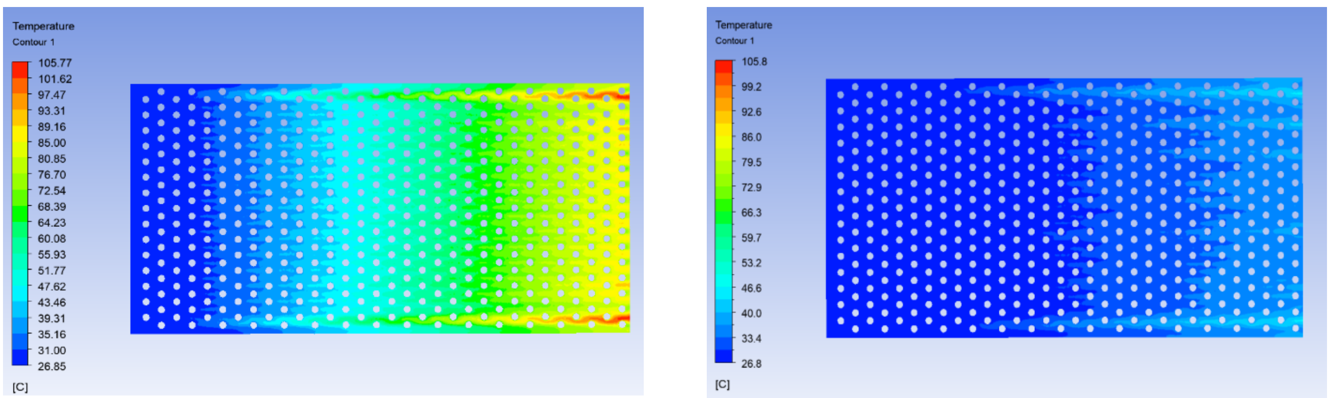

Re=3000 Re=10000

Figure 40. Contour of Temperature distribution with Re on the month of May 25 at hour 13 for the full duct configurations air solar heater

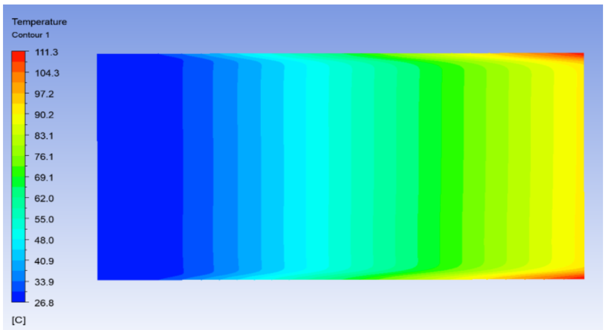

a) Smooth roughed duct

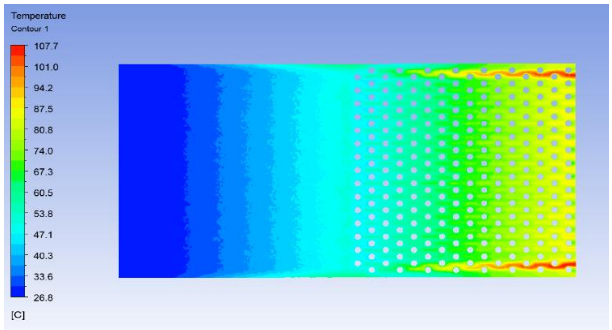

b) Right roughed duct

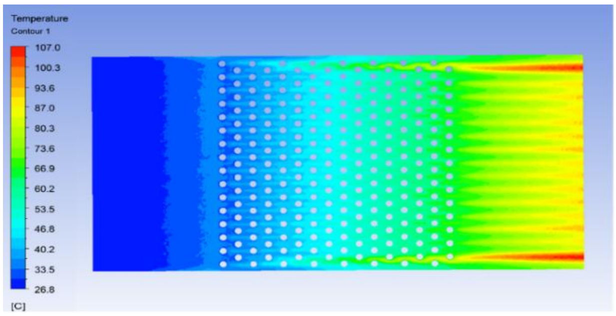

c) Middle roughed duct

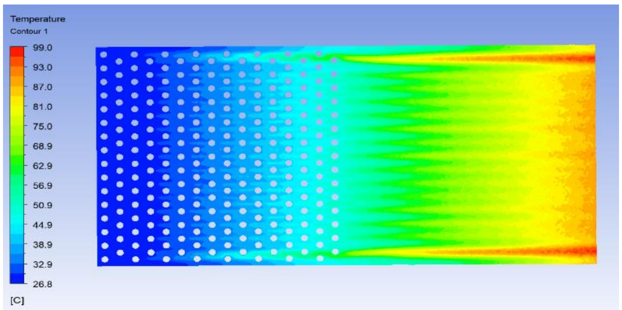

d) Left roughed duct

Figure 41. Contour of Temperature distribution with Re on the month of May 25 at hour 13 for various configurations air solar heater

a) Smooth roughed duct

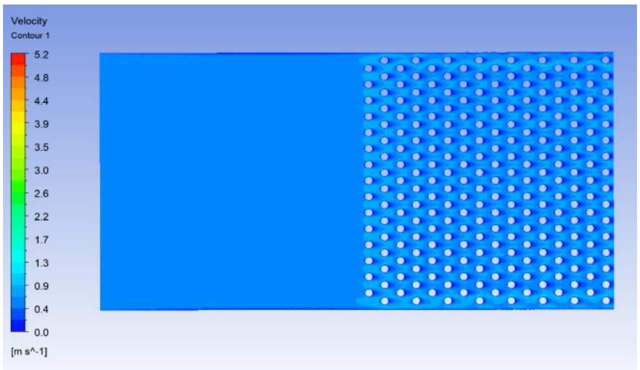

b) Right roughed duct

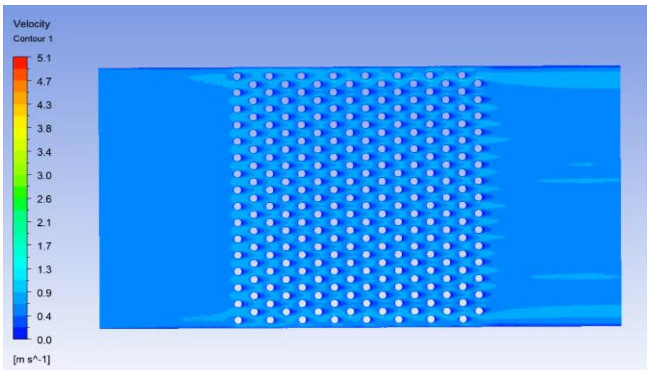

c) Middle roughed duct

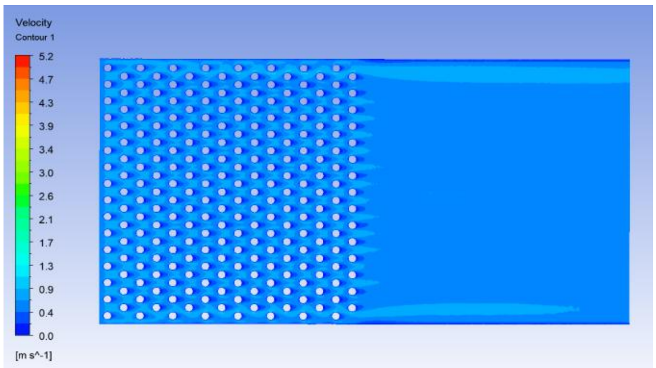

d) Left roughed duc

Figure 42. Contour of velocity distribution with Re on month of May 25 at hour 13 for various configurations of air solar heater

Table 6. Produced correlations of the experimental results as following Nu=A Re^{B} $hour^{C}$ day^{D} $month^{E}$

SAH Types	A	B	C	D	E
Empty duct case A	0.32	0.3207	0.04	0.3124	0.2741
End half duct case B	0.26	0.1408	0.0697	0.6333	0.2024
Middle half duct case D	0.195	0.4857	0.0711	0.612	0.1668
First half duct case C	0.18	0.4876	0.0882	0.7904	0.083
Full duct case E	0.15	0.477	0.106	0.9367	0.0454

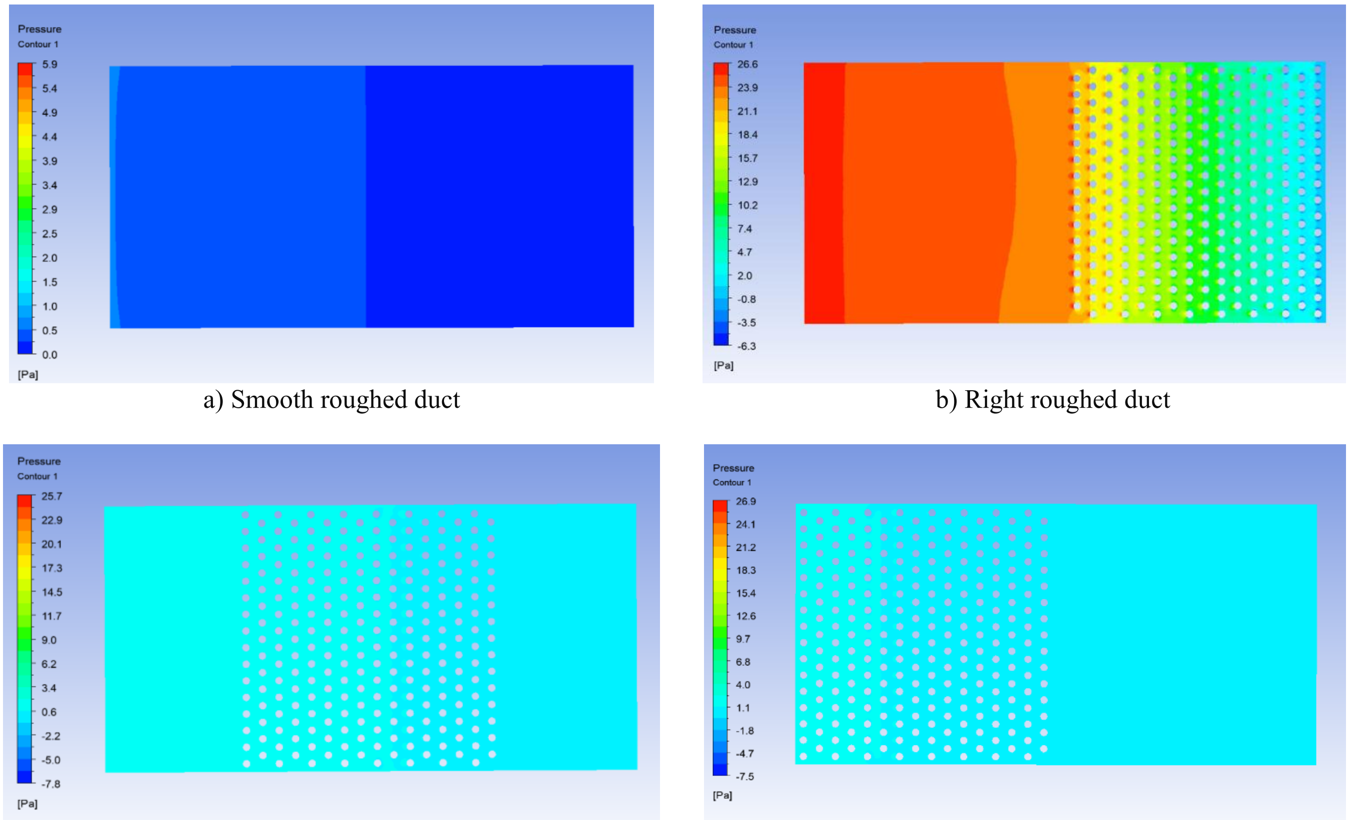

a) Smooth roughed duct   b) Right roughed duct

c) Middle roughed duct   d) Left roughed duct

Figure 43. Contour of pressure distribution with Re on month of May 25 at hour 13 for various configurations air solar heater

8. CONCLUSIONS

The examination of research on optimizing SAH performance reveals two main types of artificial roughness: ribs and baffles. Every single classification includes multiple categories based on factors including shape, size, orientation, and arrangement. Prior studies indicate a significant gap in comprehensive research concerning the positioning of baffles on the bottom plate within the air gutter of SAHs. This research study employs a three-dimensional numerical simulation. The analysis encompasses five cases: case A, representing conventional scenarios; case B, with balls positioned in the 2nd half of the air gutter (50% up); case C, featuring balls in the 1st half of the air gutter (50% down); scenario D, where balls are located in the middle of the air gutter (50% middle); and scenario E, with balls distributed throughout the entire air gutter (100%). The design and manufacturing of the ball type were thoroughly involved in this work.

The following points can be used to summarize the conclusions:

• Case E, involving 100% balls, produced the highest *Nu*.

• At the outset, the local convective HT parameter for a soft channel was higher at each Re. However, upon entering the vortex, the fluid temperature decreases, and this pattern persists throughout the channel's length.

• In the ball air channel, three distinct behaviors of the local convective HT coefficient were observed. Initially, upstream of the baffled section, small amplitude peaks are observed, indicating a low local convective HT coefficient owing to the reversed inflow of the initial balls and the prevailing inflow regime. Secondly, the baffled region exhibits large amplitude peaks, indicating a significant local convective HT coefficient resulting from the substantial vortex formations. Finally, downstream of the ball section, smaller amplitude peaks are noted, indicating a reduced local convective HT coefficient upstream.

• Cases B, C, and D exhibited nearly identical minimal values for the *f*. Because it occupies the same space from the area of the absorbent surface, was involving 100% balls.

• In all analyzed scenarios, the *f* exhibited a decrease with an increase in the Re.

• At a Re of 10,000, the *Nu* attained its peak values: 85 in example E, 70 in case C, 60 in case D, and 55 in case B, all corresponding to the same Re. At the same Re, the *Nu* exhibited a minimum value of 32 for case A. At a Re of 10,000, the maximum enhancement in *Nu* was observed as follows: Case A exhibited a 62% increase, Case C a 54% increase, Case D a 50% increase, and Case B a 41% increase.

• Correlations of the experimental results were produced for the constants of the Nu number equation for all cases as follows:

Nu=A ReB hourC dayD monthE

An analysis of heat losses resulting from convection with external air and long-wave radiation exchange with the sky has been conducted to evaluate thermal efficiency. Evidence indicates that baffles enhance efficiency, as a higher Re correlates with increased efficiency, particularly in case E (100% obstacle instance). Where the air disorder is along the plate.

ACKNOWLEDGMENT

We would like to express our sincere gratitude to the University of Technology, that have supported this work.

REFERENCES

[1] Jia, B., Liu, F., Wang, D. (2019). Experimental study on the performance of spiral solar air heater. Sol Energy, 182: 16-21. https://doi.org/10.1016/j.solener.2019.02.033

[2] Jaddoa, A.A. (2024). An empirical study of the electric solar refrigerator based on Iraqi's environment. AIP Conference Proceedings, 3002(1): 070045. https://doi.org/10.1063/5.0205774

[3] Hao, W.G., Zhang, H., Liu, S.N., Lai, Y.H. (2012). Design and prediction method of dual working medium solar energy drying system. Applied Thermal Engineering, 195: 117153. https://doi.org/10.1016/j.applthermaleng.2021.117153

[4] Zayed, M.E., Zhao, J., Elsheikh, A.H., Hammad, F.A., Ma, L., Du, Y.P., Kabeel, A.E., Shalaby, S.M. (2019). Application of cascaded phase change materials in solar water collector storage tank: A review. Solar Energy Materials and Solar Cells, 199: 24-49. https://doi.org/10.1016/j.solmat.2019.04.018

[5] Yin, Y., Chen, H., Zhao, X., Yu, W.T., Su, Hua, Chen, Y., Lin, P.C. (2022). Solar-absorbing energy storage materials demonstrating superior solar-thermal conversion and solar-persistent luminescence conversion towards building thermal management and passive illumination. Energy Conversion and Management, 266: 115804. https://doi.org/10.1016/j.enconman.2022.115804

[6] Muthukumaran, J., Senthil, R. (2022). Experimental performance of a solar air heater using straight and spiral absorber tubes with thermal energy storage. J Energy Storage, 45: 103796. https://doi.org/10.1016/j.est.2021.103796

[7] Atia, D.B., Al-Saadi, M.K., Jaddoa, A.A. (2024). Modeling of a domestic hybrid electric/solar water heating system. AIP Conference Proceedings, 3002(1): 070031. https://doi.org/10.1063/5.0206383

[8] Stelian, B.A., Croitoru, C., Bode, F., Teodosiu, C., Catalina, T. (2022). Experimental investigation of an enhanced transpired air solar collector with embodied phase changing materials. Journal of Cleaner Production, 336: 130398. https://doi.org/10.1016/j.jclepro.2022.130398

[9] Zayed, M.E., Zhao, J., Li, W., Elsheikh, A.H., Elbanna, A.M., Jing, L., Geweda, A.E. (2020). Recent progress in phase change materials storage containers: Geometries, design considerations and heat transfer improvement methods. Journal of Energy Storage, 30: 101341. https://doi.org/10.1016/j.est.2020.101341

[10] Akinbo, B.J., Olajuwon, B.I. (2020). Thermal and thermo diffusion effects on the heat and mass transfer in a viscous fluid over an exponential stretching surface in the presence of heat absorption. International Journal of Heat and Technology, 38(2): 351-360. https://doi.org/10.18280/ijht.380210

[11] El-Said, E.M.S., Gohar, M.A., Ali, A., Abdelaziz, G.B. (2022). Performance enhancement of a double pass solar air heater by using curved reflector: Experimental investigation. Applied Thermal Engineering, 202: 117867. https://doi.org/10.1016/j.applthermaleng.2021.117867

[12] Heydari, A., Mesgarpour, M. (2018). Experimental analysis and numerical modeling of solar air heater with helical flow path. Solar Energy, 162: 278-288. https://doi.org/10.1016/j.solener.2018.01.030

[13] Jaddoa, A.A. (2023). Experimental investigation of heat transfer of Supercritical fluid flowing in a tube with twisted tape. Jurnal Teknologi (Sciences & Engineering), 85(2): 69-82. https://doi.org/10.11113/jurnalteknologi.v85.18850

[14] Gopi, R., Ponnusamy, P., Fantin, A.A., Raji, A. (2021). Performance comparison of flat plate collectors in solar air heater by theoretical and computational method. Materials Today: Proceedings, 39: 823-826. https://doi.org/10.1016/j.matpr.2020.09.809

[15] Chitsazan, A., Glasmacher, B. (2020). Numerical investigation of heat transfer and pressure force from multiple jets impinging on a moving flat surface. International Journal of Heat and Technology, 38(3): 601-610. https://doi.org/10.18280/ijht.380304

[16] Nain, S., Ahlawat, V., Kajal, S., Anuradha, P., Sharma, A., Singh, T. (2021). Performance analysis of different U-shaped heat exchangers in parabolic trough solar collector for air heating applications. Case Studies in Thermal Engineering, 25: 100949. https://doi.org/10.1016/j.csite.2021.100949

[17] Perwez, A., Kumar, R. (2019). Thermal performance investigation of the flat and spherical dimple absorber plate solar air heaters. Solar Energy, 193: 309-323. https://doi.org/10.1016/j.solener.2019.09.066

[18] Jaddoa, A.A., Mahdi Mahmoud, M., Hamad Karema, A. (2023). On assessing the effectiveness of hybrid solar collectors scheme in Iraq's environment. Eurasian Physical Technical Journal, 20(2): 57. https://doi.org/10.31489/2023No2/57-64

[19] Jiang, Y., Zhang, H., Wang, Y., You, S., Wu, Z., Fan, M., Wang, L., Wei, S. (2021). A comparative study on the performance of a novel triangular solar air collector with tilted transparent cover plate. Solar Energy, 227: 224-235. https://doi.org/10.1016/j.solener.2021.08.083

[20] Al-Obaidi, A.R., Alhamid, J. (2021). Investigation of thermo-hydraulics flow and augmentation of heat transfer in the circular pipe by combined using corrugated tube with dimples and fitted with varying tape insert configurations. International Journal of Heat and Technology, 39(2): 365-374. https://doi.org/10.18280/ijht.390205

[21] Zhang, H., Ma, X., You, S., Wang, Y., Zheng, X., Ye, T., Zheng, W., Wei, S. (2018). Mathematical modeling and performance analysis of a SAH with silt-perforated corrugated plate. Solar Energy, 167: 147-157. https://doi.org/10.1016/j.solener.2018.04.003

[22] Saedodin, S., Zaboli, M., Ajarostaghi, S.S.M. (2021). Hydrothermal analysis of heat transfer and therma performance characteristics in a parabolic trough solar collector with Turbulence-Inducing elements. Sustainable Energy Technologies and Assessments, 46: 101266. https://doi.org/10.1016/j.seta.2021.101266

[23] Mahdi, M.M., Jaddoa, A.A., Al Ezzi, A. (2022). Impact of pumping head on a solar pumping system with an optimal PV array configuration: solar water heater

application, Journal of Engineering Science and Technology, 17(3): 2035-2048.
[24] Chand, S., Chand, P., Kumar, G.H. (2022). Thermal performance enhancement of solar air heater using louvered fins collector. Solar Energy, 239: 10-24. https://doi.org/10.1016/j.solener.2022.04.046
[25] Rehman, T., Nguyen, D.D., Sajawal, M. (2024). Smart optimization and investigation of a PCMs- filled helical finned-tubes double-pass solar air heater: An experimental data-driven deep learning approach. Thermal Science and Engineering Progress, 49: 102433. https://doi.org/10.1016/j.tsep.2024.102433
[26] Saravanakumar, P.T., Somasundaram, D., Matheswaran, M.M. (2020). Exergetic investigation and optimization of arc shaped rib roughened solar air heater integrated with fins and baffles. Applied Thermal Engineering, 175: 115316. https://doi.org/10.1016/j.applthermaleng
[27] Jaddoa, A.A. (2021). Convection heat transfer performance for the SCF-CO_2 media in mini- tube with fins experimentally. Journal of Engineering Science and Technology, 16(4): 3407-3420.
[28] Marwa, A., Ameni, M., Hatem, M., Bournot, P. (2020) Numerical analysis of SAH provided with rows of rectangular fins. Energy Reports, 6: 3412-3424. https://doi.org/10.1016/j.egyr.2020.11.252
[29] Aref, L., Fallahzadeh, R., Shabanian, S.R., Hosseinzadeh, M. (2021). A novel dual-diameter closed-loop pulsating heat pipe for a flat plate solar collector. Energy, 230: 120751. https://doi.org/10.1016/j.energy.2021.120751
[30] Saravanan, A., Murugan, M., Sreenivasa, R.M., Ranjit, P.S., Elumalai, P.V., Kumar, P., Rama Sree, S. (2021). Thermo-hydraulic performance of a solar air heater with staggered C-shape finned absorber plate. International Journal of Thermal Sciences, 168: 107068. https://doi.org/10.1016/j.ijthermalsci.2021.107068
[31] Du, J., Chen, H., Li, Q., Huang, Y., Hong, Y. (2024). Turbulent flow-thermal-thermodynamic characteristics of a solar air heater with spiral fins. International Journal of Heat and Mass Transfer, 226: 125434. https://doi.org/10.1016/j.ijheatmasstransfer.2024.125434
[32] Elumalai, V., Arunkumar, T., Thiruselvam, K., Senthil, S. (2021). Thermal performance improvement in solar air heating: An absorber with continuous and discrete tubular and v-corrugated fins. Thermal Science and Engineering Progress, 48: 102416. https://doi.org/10.1016/j.tsep.2024.102416
[33] Waheed, S., Mahamed, E., Ravishankar, S., Moustafa, E.B., Elsheikh, A.H. (2023). Performance evaluation of a solar air heater with staggered/longitudinal finned absorber plate integrated with aluminium sponge porous medium. Journal of Building Engineering, 73: 106841. https://doi.org/10.1016/j.jobe.2023.106841
[34] Amraoui, M.A. (2021). Three-dimensional numerical simulation of a flat plate solar collector with double paths. International Journal of Heat and Technology, 39(4): 1087-1096. https://doi.org/10.18280/ijht.390406
[35] Wang, L., Man, Y. (2018). Numerical simulation of SAH with folded baffles. Renewable Energy Resources, 36(7): 997-1003. https://doi.org/10.13941/j.cnki.21-1469/tk.2018.07.008
[36] Jia, B., Yang, L., Zhang, L., Liu, B., Liu, F., Li, X. (2021). Optimizing structure of baffles on thermal performance of spiral solar air heaters. Solar Energy, 224: 757-764. https://doi.org/10.1016/j.solener.2021.06.043
[37] Mondal, R.N., Hasan, M.S., Islam, M.S., Islam, M.Z., Saha, S.C. (2021). A computational study on fluid flow and heat transfer through a rotating curved duct with rectangular cross section. International Journal of Heat and Technology, 39(4): 1213-1224. https://doi.org/10.18280/ijht.390419
[38] Rani, P., Tripathy, P.P. (2022). Experimental investigation on heat transfer performance of solar collector with baffles and semicircular loops fins under varied air mass flow rates. International Journal of Thermal Sciences, 178: 107597. https://doi.org/10.1016/j.ijthermalsci.2022.107597
[39] Jia, B., Liu, F., Li, X., Qu, A., Cai, Q. (2021) Influence on thermal performance of spiral solar air heater with longitudinal baffles. Solar Energy, 225: 969-977. https://doi.org/10.1016/j.solener.2021.08.004
[40] Zayed, M.E., Kabeel, A., Bashar, S., Ashraf, W.M., Ghazy, M., Irshad, K., Rehman, S., Zayed, A.A.A. (2023) Performance augmentation and machine learning- based modeling of wavy corrugated solar air collector embedded with thermal energy storage: Support vector machine combined with Monte Carlo simulation. Journal of Energy Storage, 74: 109533. https://doi.org/10.1016/j.est.2023.109533
[41] Jaddoa, A.A., Ekaid, A.L., Al-Sadawi, L. (2020). A numerical study of natural convection in square cavity with heated cylinder of different diameter and location through computational analysis. Journal of Engineering Science and Technology, 15(4): 2472-2491.
[42] Magda, K., Aly-Eldeen, A., Abdelmaqsoud, A., Marzouk, S.A. (2024) Enhanced performance assessment of an integrated evacuated tube and flat plate collector solar air heater with thermal storage material. Applied Thermal Engineering, 245: 122653. https://doi.org/10.1016/j.applthermaleng.2024.122653
[43] Wang, L. (2022). Research on the collect heat performance of new type collector. Energy Sources, Part A: Recovery, Util, Environ Effects, 44(4): 9412-9427. https://doi.org/10.1080/15567036.2021.1954729
[44] Song, Z., Xue, Y., Jia, B., He, Y. (2022) Introduction of the rectangular hole plate in favor the performance of photovoltaic thermal solar air heaters with baffles. Applied Thermal Engineering, 220: 119774. https://doi.org/10.1016/j.applthermaleng.2022.119774
[45] Mahdi, M.M., Jaddoa, A.A. (2021). An experimental optimization study of a photovoltaic solar pumping system used for solar domestic hot water system under Iraqi climate. Journal of Thermal Engineering, 7(2): 162-173. https://doi.org/10.18186/thermal.871296
[46] Zhang, D., Zhang, J.J., Zhang, Y.Z., Wang, L.J. (2019) Baffles optimization of a flat plate SAH with double channel. Journal of Shanghai Jiaotong University, 53(11): 1302-1307. https://doi.org/10.16183/j.cnki.jsjtu.2019.11.005